(19) 4606T, AD-E300 389

(12) LEVEL II

(18) DNA 4606T

SBIE

AD A062333

(6)

ON THE INTERPRETATION OF IONOSPHERIC SCINTILLATION DATA USING A POWER-LAW PHASE SCREEN MODEL--WEAK SCATTER

SRI International
333 Ravenswood Avenue
Menlo Park, California 94025

(10) Charles L. Rino
Stephen J. Matthews

(12) 61p.

(11) Feb[redacted]78

(9) Topical Report no. 2, [redacted] 1 Jun[redacted]77–28 Feb[redacted]78

CONTRACT No. DNA 001-77-C-0220

(15)

APPROVED FOR PUBLIC RELEASE;
DISTRIBUTION UNLIMITED.

THIS WORK SPONSORED BY THE DEFENSE NUCLEAR AGENCY
UNDER RDT&E RMSS CODE B322078462 I25AAXHX63340 H2590D.

(16)

Prepared for
Director
DEFENSE NUCLEAR AGENCY
Washington, D. C. 20305

(17) X633

410 281

78

Destroy this report when it is no longer needed. Do not return to sender.

PLEASE NOTIFY THE DEFENSE NUCLEAR AGENCY, ATTN: TISI, WASHINGTON, D.C. 20305, IF YOUR ADDRESS IS INCORRECT, IF YOU WISH TO BE DELETED FROM THE DISTRIBUTION LIST, OR IF THE ADDRESSEE IS NO LONGER EMPLOYED BY YOUR ORGANIZATION.

UNCLASSIFIED

SECURITY CLASSIFICATION OF THIS PAGE (When Data Entered)

REPORT DOCUMENTATION PAGE

READ INSTRUCTIONS BEFORE COMPLETING FORM

1. REPORT NUMBER: DNA 4606T	2. GOVT ACCESSION NO.
3. RECIPIENT'S CATALOG NUMBER	
4. TITLE (and Subtitle): ON THE INTERPRETATION OF IONOSPHERIC SCINTILLATION DATA USING A POWER-LAW PHASE SCREEN MODEL--WEAK SCATTER	5. TYPE OF REPORT & PERIOD COVERED: Topical Report 2 for Period 1 June 1977—28 February 1978
	6. PERFORMING ORG. REPORT NUMBER: SRI Project 6434
7. AUTHOR(s): Charles L. Rino, Stephen J. Matthews	8. CONTRACT OR GRANT NUMBER(s): DNA 001-77-C-0220
9. PERFORMING ORGANIZATION NAME AND ADDRESS: SRI International, 333 Ravenswood Avenue, Menlo Park, California 94025	10. PROGRAM ELEMENT, PROJECT, TASK AREA & WORK UNIT NUMBERS: Subtask I25AAXHX633-40
11. CONTROLLING OFFICE NAME AND ADDRESS: Director, Defense Nuclear Agency, Washington, D.C. 20305	12. REPORT DATE: February 1978
	13. NUMBER OF PAGES: 62
14. MONITORING AGENCY NAME & ADDRESS (if different from Controlling Office)	15. SECURITY CLASS (of this report): UNCLASSIFIED
	15a. DECLASSIFICATION/DOWNGRADING SCHEDULE

16. DISTRIBUTION STATEMENT (of this Report)

Approved for public release; distribution unlimited.

62710H

17. DISTRIBUTION STATEMENT (of the abstract entered in Block 20, if different from Report)

18. SUPPLEMENTARY NOTES

This work sponsored by the Defense Nuclear Agency under RDT&E RMSS Code B322078462 I25AAXHX63340 H2590D.

19. KEY WORDS (Continue on reverse side if necessary and identify by block number)

Scintillation
Striations
Phase-Screen Model

S sub 4 as < or approximately

20. ABSTRACT (Continue on reverse side if necessary and identify by block number)

An equivalent phase screen model is used to interpret the Wideband satellite data under conditions of weak scattering where the intensity scintillation is such that $S_4 \lesssim 0.4$. The phase spectral density is fitted to a power-law model of the form Tf^{-p} to obtain the basic parameters T and p. The phase screen model is then used to remove the geometrical dependence of T. An invariant strength-of-turbulence parameter can be obtained from

DD FORM 1 JAN 73 1473 EDITION OF 1 NOV 65 IS OBSOLETE

Tf (to the -p power)

UNCLASSIFIED

SECURITY CLASSIFICATION OF THIS PAGE (When Data Entered)

78 10 30 103

20. ABSTRACT (Continued)

Such an analysis. By using the phase-screen model, the Wideband rms phase and intensity data have been self-consistently calculated, thereby verifying the validity of the model. The results are used to calculate the rms electron density perturbation levels required to produce significant gigahertz scintillation.

ACCESSION for	
NTIS	White Section ☑
DDC	Buff Section ☐
UNANNOUNCED	☐
JUSTIFICATION	
BY	
DISTRIBUTION/AVAILABILITY CODES	

Dist.	AVAIL. and/or SPECIAL	
A		

EXECUTIVE SUMMARY

The Wideband Satellite data presently constitute the most extensive collection of global intensity and phase scintillation data available. The data are being used to evaluate the scintillation-induced performance degradation in a variety of systems. For a low orbiting satellite such as Wideband, however, the structure of the scintillation data is critically dependent on the propagation geometry. Thus, to use the Wideband satellite data effectively, we must have a model to separate the purely geometrical effects from the true source variations.

In this report we show that an appropriately located equivalent phase-changing screen accurately reproduces the measured phase and intensity scintillation from individual Wideband passes. We assume that the three-dimensional spectral density of the ionospheric irregularities has the form $C_s\kappa^{-(2\nu+1)}$. The spectral index parameter ν and the strength of turbulence C_s are determined by using the model calculations and the summary parameters that are routinely obtained from the phase scintillation data by fitting a curve of the form Tf^{-p} to the measured phase spectral density function.

The measured average p index values fall in the range $2 < p < 3$; however, the data show a systematic difference between the auroral zone and the equator. For the auroral-zone data, the p indices are generally smaller and more variable than the p indices for the equatorial data, which give values closer to the nominal value $p = 3$. Nonetheless, the Kwajalein data give somewhat smaller p values than the Ancon data.

The free parameters in the phase-screen model are the height of the phase screen and the irregularity axial ratios along and transverse to the magnetic field. We have assumed that the satellite scan velocity, which is known, dominates the irregularity drift component. Self-consistent fits to the measured rms phase and S_4 generally require the equivalent phase screen to be in the F region for both the auroral and equatorial data.

The equatorial data are consistent with rod-like irregularities with a minimum axial ratio of 20:1. The auroral-zone data are generally consistent with sheet-like structures aligned along L-shells at least for propagation paths within the auroral oval. A detailed analysis of the irregularity anisotropy is being independently pursued by using the Wideband spaced receiver data.

The phase-screen formulas have been greatly simplified by taking limits as the outer scale approaches infinity and the inner scale approaches zero. The justification for using these approximations is that no evidence of systematic departures from the power-law spectral form has been found in either the Wideband data or any other reported phase scintillation data. Thus, the cutoff scales are outside the range of the scale sizes that affect the data, and they are properly excluded from the analysis.

We have also used the estimated turbulence levels to determine the rms electron density perturbation that would be measured by an in-situ probe. We have found, for example, that significant gigahertz scintillation can be accounted for by purturbations with rms electron density levels between 10^{11} el/m^3 and 10^{12} el/m^3 over a 200-km propagation path. Smaller levels distributed over a larger path would, of course, produce the same result.

CONTENTS

ILLUSTRATIONS

I INTRODUCTION

Phase changing screens have been used to model optical and radio-wave scintillation phenomena throughout the development of the theory of scintillation (Booker et al., 1950; Bramley, 1954; Ratcliffe, 1956; Salpeter, 1967; Cronyn, 1970; Rufenach, 1975; Rumsey, 1975; Buckley, 1975). The phase-screen model is appealing because of its conceptual and analytical simplicity. It is often argued, however, that the phase-screen model cannot accurately describe scintillation data because non-negligible amplitude variations invariably develop within the scattering medium (see for example Wernik, 1976; Crane, 1977).

While such arguments are essentually correct, one feels intuitively that an appropriately located equivalent phase screen should accurately reproduce the average properties of scintillations that develop both within and beyond an extended medium. Indeed, Bramley (1977) has recently demonstrated by direct computation that such an equivalent phase screen is surprisingly accurate. For irregularities with a power-law spectral distribution, Bramley's calculations show that the errors made in computing the amplitude and phase scintillation levels by using an equivalent phase screen amount to only a few percent even if the receiver lies within the scattering medium.

In this report we shall demonstrate that the phase-screen model accurately reproduces both the level and the propagation geometry dependence of ionospheric scintillation data obtained from the Wideband satellite. Data have been acquired from auroral zone and equatorial stations. The auroral-zone data present a complicated, rapidly changing propagation geometry combined with extreme source variations. The equatorial data provided examples of the gigahertz scintillation phenomena that have recently received considerable attention (Basu et al., 1976; Costa and Kelley, 1976).

We shall consider only weak scattering in this report. This is not overly restrictive because saturated scintillation at L-band is observed only occasionally. Nonetheless, even under conditions of strong scattering, the phase-screen model remains the simplest means of obtaining flexible yet tractable results, particularly in a power-law scattering environment (Gochelashvili and Shishov, 1971; Taylor, 1972; and Rumsey, 1975).

Phase scintillation data are used in the model calculations essentially to determine the rms phase level for the phase-changing screen. Indeed, the potential of differential phase measurements has been recognized for some time as an accurate means of measuring relative and absolute total (integrated) electron content (TEC) (Leitinger et al., 1975).

The principle of the differential phase technique is simply that large-scale phase variations are directly proportional to wavelength times the TEC along the propagation path. The more rapidly changing phase scintillations can be thought of as TEC noise. To some extent, diffraction effects must ultimately upset the simple proportionality between phase and wavelength times TEC. An important finding from the Wideband data is that under conditions of weak scattering, diffraction effects in the phase data are negligible to time scales substantially shorter than the characteristic intensity fading period.

If diffraction effects were indeed important, one would expect the phase scintillation to be sensitive to changes in Fresnel radius and thus vary nonlinearly with wavelength. Yet, we have consistently observed a nearly linear wavelength dependence of rms phase except under the most severe scattering conditions (Fremouw et al., 1978). We conclude that under conditions of weak scattering the diffraction effects in the phase data can be largely ignored. We shall demonstrate this in Section II by comparing simultaneously recorded phase data at different frequencies.

A second important finding in both the Wideband data and other differential phase measurements (Crane, 1976) is that the differential phase spectrum admits a power-law representation with no intrinsic low-frequency cutoff (outer scale). The range of the power-law continuum has recently been discussed by Yeh and Liu (1977). The fact that we are dealing with a power-law continuum with an inaccessible outer scale has important consequences for data interpretation. Indeed, neither an inner scale nor an outer-scale cutoff has been detected in any scintillation data reported to date. It follows that such parameters need not enter a properly formulated scintillation theory.

The inner-scale cutoff does not affect the amplitude or phase scintillation data because it occurs well below the noise level. In the Appendix we present a simple formula that allows us to correct the intensity scintillation index S_4 for noise contamination. No correction is necessary for the phase data.

If the outer-scale cutoff is large compared to the Fresnel radius, the diffraction process removes any influence that large scale structure might have in the intensity scintillation data. In the phase data the detrending procedure that is used to remove TEC-induced slow phase trends dictates the low-frequency cutoff of the spectrum. Under conditions of both weak and strong scattering, Fresnel filtering introduces an intrinsic low-frequency cutoff in intensity scintillation data. Thus, since the outer scale has not been detected in phase scintillation data, it follows a fortiori that the outer scale has no direct influence on intensity scintillation data. We shall see in Section III that if one takes this fact into account at the outset, the theory is considerably simplified.

In Section IV we apply the power-law phase-screen theory to Wideband equatorial and auroral data. We show that whenever the model accurately reproduces the rms phase data, there is a set of anisotropy parameters and an equivalent phase screen height that will accurately reproduce the measured S_4 values as long as $S_4 \lesssim 0.4$ For larger S_4 values the weak-scatter theory overestimates S_4.

By using the phase-screen model we can estimate the in-situ rms electron density perturbation level that is consistent with the scintillation data. In Section V we show that gigahertz scintillation can be easily explained with rms electron density perturbations between 10^{11} el/m^3 and 10^{12} el/m^3 distributed over a 200-km layer.

II PHASE SCINTILLATION

In this section we shall first review a general model that completely characterizes the structure of the phase scintillation exclusive of diffraction effects. We shall then compute the form of the one-dimensional phase power spectrum, which can actually be measured. From the form of the phase power spectrum we deduce the relationship that converts the measured power in a given frequency interval to an electron density perturbation level in the corresponding spatial frequency regime.

We also calculate the form of the measurable rms phase and discuss the consequences of the inaccessible outer scale wavenumber. Finally, we present some examples that show the extent to which diffraction effects are detectable in phase data under conditions of weak scattering.

The zeroth-order approximation to the differential phase $\delta\phi$ is given by the integral along the propagation path

$$\delta\phi = -r_e\lambda \int \Delta N_e \, d\ell \left(1 - (f/f_r)^2\right) + \text{terms that depend on } \lambda z \tag{1}$$

where r_e is the classical electron radius, λ is the wavelength ($f\lambda = c$, where c is the velocity of light), f_r is the reference frequency, and ΔN_e is the local electron density perturbation. For the moment, let us assume that f_r is infinite and that λz-dependent terms in Eq. (1) are indeed negligible.

In Rino and Fremouw (1977) it is shown that the phase autocorrelation function derived from Eq. (1) has the general form

$$R_{\delta\phi}(\Delta\vec{\rho}_s) = r_e^2\lambda^2 L \sec^2\theta \iint \Phi_{\Delta N_e}(\vec{K}, -\tan\theta \, \hat{a}_{k_T} \cdot \vec{K}) \cos(\vec{K} \cdot \Delta\vec{\rho}_s) \frac{d\vec{K}}{(2\pi)^2} \tag{2}$$

where L is the layer thickness

$$\Delta\vec{\rho}_s = \Delta\vec{\rho} - \tan\theta \, \hat{a}_{k_T} \Delta z \tag{3}$$

and

$$\hat{a}_{k_T} = (\cos\varphi, \sin\varphi) \quad . \tag{4}$$

The angles θ and φ are, respectively, the zenith and magnetic azimuth angles of the propagation vector $\vec{k}$. We note that $\hat{a}_{k_T}$ lies along the horizontal projection of $\vec{k}$. The z axis of the reference coordinate system is downward-directed and the xz plane contains the local geomagnetic meridian.

We note that Eq. (2) is a fully three-dimensional characterization of the phase structure. The Δz dependence is contained in $\Delta\vec{\rho}_s$. In Eq. (2) $\Phi_{\Delta N_e}(\vec{\kappa},\kappa_z)$ is the three-dimensional spectral-density function (SDF) of the irregularities. In Rino and Fremouw (1977), it is shown that for a fairly general anisotropy model, the SDF in Eq. (2) has the form

$$\Phi_{\Delta N_e}(\vec{\kappa}, -\tan\theta\ \hat{a}_{k_T}\cdot\vec{\kappa}) = ab\ \langle\Delta N_e^2\rangle\ Q\ (A\kappa_x^2 + B\kappa_x\kappa_y + C\kappa_y^2) \quad . \tag{5}$$

The parameters a and b are axial ratios along and transverse to the principal irregularity axis. The coefficients A, B, and C depend on the propagation angles relative to the principal irregularity axis (see Eq. (41) in Rino and Fremouw, 1977).

The function Q(q) gives the shape of the SDF. It is normalized so that $\int_0^\infty q\ Q(q)\ dq/(2\pi^2) = 1$. Thus, for a power-law SDF we can take

$$Q(q) = \frac{8\pi^{3/2}\ \Gamma(\nu + 1/2)/\Gamma(\nu - 1)q_o^{2\nu-2}}{[q_o^2 + q^2]^{\nu + 1/2}} \quad . \tag{6}$$

If we make the definition

$$C_s = 8\pi^{3/2}\ \langle\Delta N_e^2\rangle q_o^{2\nu-2}\ \Gamma(\nu + 1/2)/\Gamma(\nu - 1) \tag{7}$$

it follows that $\Phi_{\Delta N_e}(\vec{\kappa},\kappa z) = C_s\kappa^{-(2\nu+1)}$ for $\kappa \gg q_o$. The parameter C_s will be referred to as the strength of turbulence.

Now, if we substitute Eq. (5) and Eq. (6) into Eq. (2) and change variables, the result is

$$R_{\delta\phi}(y) = r_e^2\lambda^2 L \sec\theta\, G\, C_s \int_0^\infty \frac{q\, J_o\,(qy)}{[q_o^2 + q^2]^{\nu+1/2}}\, dq/2\pi \tag{8}$$

where

$$G = \frac{ab}{\sqrt{AC - B^2/4}\,\cos\theta} \tag{9}$$

and y is replaced by $f(\Delta\vec{\rho}_s)$ where

$$f^2(\Delta\vec{\rho}_s) = \frac{C\Delta\rho_{s_x}^{\;2} - B\Delta\rho_{s_x}\Delta\rho_{s_x} + A\Delta\rho_{s_x}^{\;2}}{AC - B^2/4}\ . \tag{10}$$

A discussion of Eq. (8) that describes its relation to the Briggs and Parkin (1963) formulation is given in Rino and Fremouw (1977).

The integral in Eq. (8) can be evaluated giving the result

$$R_{\delta\phi}(y) = r_e^2\lambda^2 L \sec\theta\, G\, C_s\, \frac{q_o^{-(\nu-1/2)}\, y^{\nu-1/2} K_{\nu-1/2}(q_o y)}{2\pi\, 2^{\nu-1/2}\,\Gamma(\nu + 1/2)} \tag{11}$$

where $K_\nu(x)$ is the modified Bessel function. In an actual experiment, we would measure a temporal autocorrelation of the form $R_{\delta\phi}(v_{eff}\,\delta t)$ where

$$v_{eff} = \left[\frac{Cv_{s_x}^2 - Bv_{s_x}v_{s_y} + Av_{s_y}^2}{AC - B^2/4}\right]^{1/2} \tag{12}$$

and

$$\vec{v}_s = \vec{v}_T - \tan\theta\,\hat{a}_{k_T}\, v_z\ . \tag{13}$$

Finally, $\vec{v} = (\vec{v}_T, v_z)$ is the relative scan velocity at the ionospheric penetration point induced by both the source motion and the irregularity drifts. The effective scan velocity parameter v_{eff} cannot be larger than v. However, v_{eff} can be substantially smaller than v--for example, if the scan direction is along the principal irregularity.

Let us now consider the temporal power spectrum of phase which is defined by the expression

$$\varphi(f) = \int_{-\infty}^{\infty} R_{\delta\phi}(v_{eff}\,\delta t)\,\cos\,(2\pi i f \delta t)\; d\,\delta t\ . \qquad (14)$$

Substituting Eq. (11) into Eq. (14) and evaluating the integral gives

$$\varphi(f) = r_e^2 \lambda^2 L \sec\theta\ G\ C_s \frac{\Gamma(\nu)}{2\sqrt{\pi}\ \Gamma(\nu+1/2)\ v_{eff}} \frac{1}{[q_o^2 + (2\pi f/v_{eff})^2]^{\nu}}\ . \qquad (15)$$

Now, recalling the definition of the C_s parameter [Eq. (7)], we make the analogous definition

$$T = r_e^2 \lambda^2 (L \sec\theta)\ G\ C_s \frac{\sqrt{\pi}\ \Gamma(\nu)}{(2\pi)^{2\nu+1}\ \Gamma(\nu+1/2)}\ v_{eff}^{\ 2\nu-1} \qquad (16)$$

so that whenever $(2\pi f/v_{eff}) \gg q_o$, $\varphi(f) = Tf^{-2\nu}$. As a check on the computations, we note that the spectral index of the one-dimensional phase spectrum, 2ν, is one less than the corresponding spectral index of the three-dimensional irregularity spectrum, $2\nu+1$ [see Eq. (6)]. Equation (16) shows that the phase scintillation level depends critically on the propagation geometry, particularly through G and v_{eff}, as well as the relative scan velocity $\vec{v}$.

To continue, we note that a detrending procedure (essentially a high-pass filter) must be applied to separate the slow TEC-induced trend-like phase variations from the more rapid phase scintillations. It is this detrending procedure that dictates the smallest measurable temporal frequency component in $\varphi(f)$--say, f_c. Since we have found no systematic intrinsic cutoff cutoff in the spectrum, we must conclude that the inequality $(2\pi f_c/v_{eff}) \gg q_o$ always holds. It follows that the only unambiguous characterization of the phase spectrum is in terms of the parameters T and $p = 2\nu$, which are routinely measured in the Wideband data reduction (Fremouw et al., 1978).

The consequences of this fact are important. First, no absolute value or even upper bound can be assigned to the phase variance. The measured phase variance is reasonably well approximated by the formula

$$\langle \delta\hat{\phi}^2 \rangle \cong T \int_{\infty}^{\infty} \frac{df}{[f_c^2 + f^2]^{p/2}} = T\, f_c^{-p+1} \frac{\sqrt{\pi}\, \Gamma(\nu-1/2)}{\Gamma(\nu)} \quad . \tag{17}$$

From Eq. (16) and Eq. (17) it follows that

$$\langle \delta\hat{\phi}^2 \rangle \propto \lambda^2 (L \sec\theta)\, G\, v_{eff}^{(p-1)} \quad . \tag{18}$$

Now, if we take the limit of Eq. (11) as $y \to 0$ or integrate $\Phi(f)$ over all frequencies, we obtain the ideal phase variance

$$\langle \delta\phi^2 \rangle = r_e^2 \lambda^2 \,(L \sec\theta)\, G\, C_s \frac{q_o^{-2\nu+1}\, \Gamma(\nu-1/2)}{4\pi\, \Gamma(\nu+1/2)} \tag{19}$$

which is the conventional rms phase expression.

To properly interpret ionospheric phase scintillation data, Eq. (18) must be used. The principal difference between Eqs. (18) and (19) is the dependence of the former on v_{eff}. Indeed, v_{eff} depends critically on altitude. Hence, the measured rms phase will also depend on altitude.

To summarize, an unambiguous characterization of phase scintillation data can be obtained only in terms of the spectral strength parameter T and the spectral index p. If we can estimate the anisotropy and drift of the ionospheric irregularities, Eq. (16) can be used to estimate the strength of turbulence C_s which, as with T itself, is presently the only unambiguous average parameter that can be used to characterize the spectral strength of the ionospheric irregularities.

We have assumed in this analysis that diffraction effects in the phase data are negligible. In Fremouw et al. (1978), it is shown that the measured rms phase, when corrected for the finite reference frequency [Eq. (11)], varies linearly with wavelength. We shall now show that under conditions of weak scatter the detailed structure of the phase itself scales with frequency as predicted by Eq. (1) to periods shorter than one second.

In Figure 1 we show a typical VHF phase scintillation record. The raw phase data have been detrended to remove phase variations with periods greater than 10 s (f_c = 0.1 Hz). Before 0920 UT the S_4 scintillation index is less than 0.4. In Figure 2 we show on an expanded scale the differences between the phase at the indicated lower frequencies and the scaled phase at the indicated higher frequencies. The designations UL3 and UU3 denote, respectively, the lowest and highest of seven equispaced UHF frequencies. One can see that prior to 0920 UT the large-scale phase variations are completely suppressed, and therefore unaffected by diffraction.

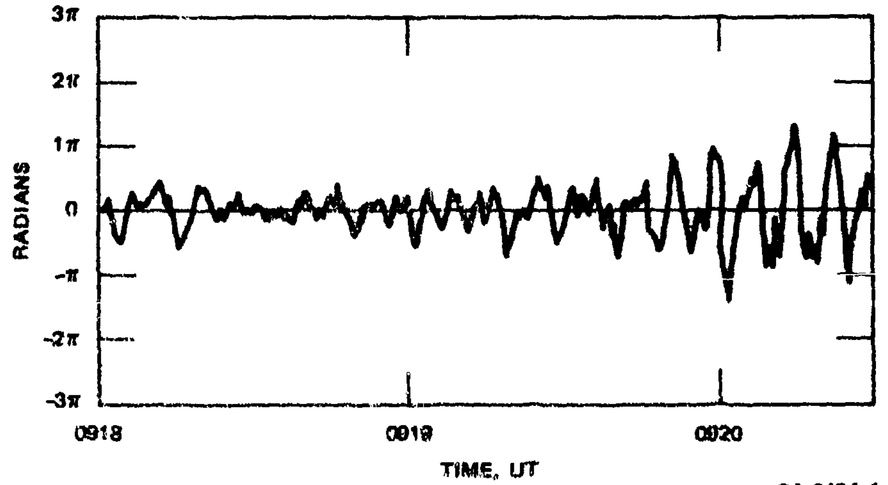

FIGURE 1 SEGMENT OF DETRENDED PHASE DATA (f_c = 0.1 Hz) FROM WIDEBAND PASS 6-35 RECORDED AT POKER FLAT, ALASKA

To demonstrate this quantitatively, in Figure 3 we show the VHF phase spectrum and the spectrum of the VHF-UU3 phase difference. Below 1 Hz there is essentially 20 dB of cancellation. Beyond 30 Hz, the phase difference spectrum is ~ 3 dB above the VHF phase spectrum indicating total decorrelation. We see that the diffraction effects are largely confined to frequencies greater than 1 Hz. However, the dominant spectral content comes from frequencies below 1 Hz, which explains why the rms phase follows the linear wavelength dependence so accurately.

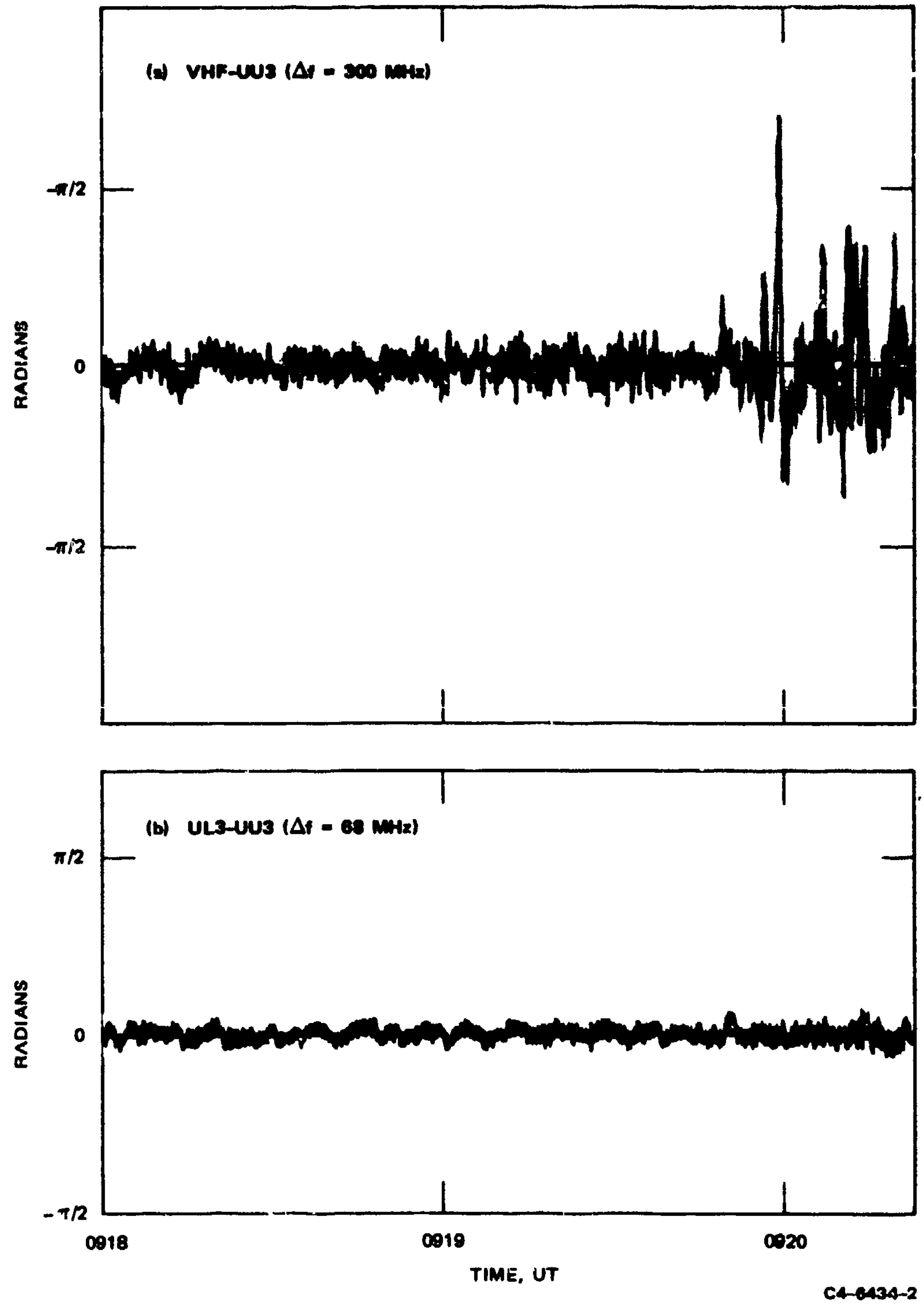

FIGURE 2 DIFFERENCE BETWEEN MEASURED PHASE AT LOW FREQUENCY AND SCALED PHASE FROM HIGHER FREQUENCY FOR SEGMENT OF POKER FLAT PASS 6-36

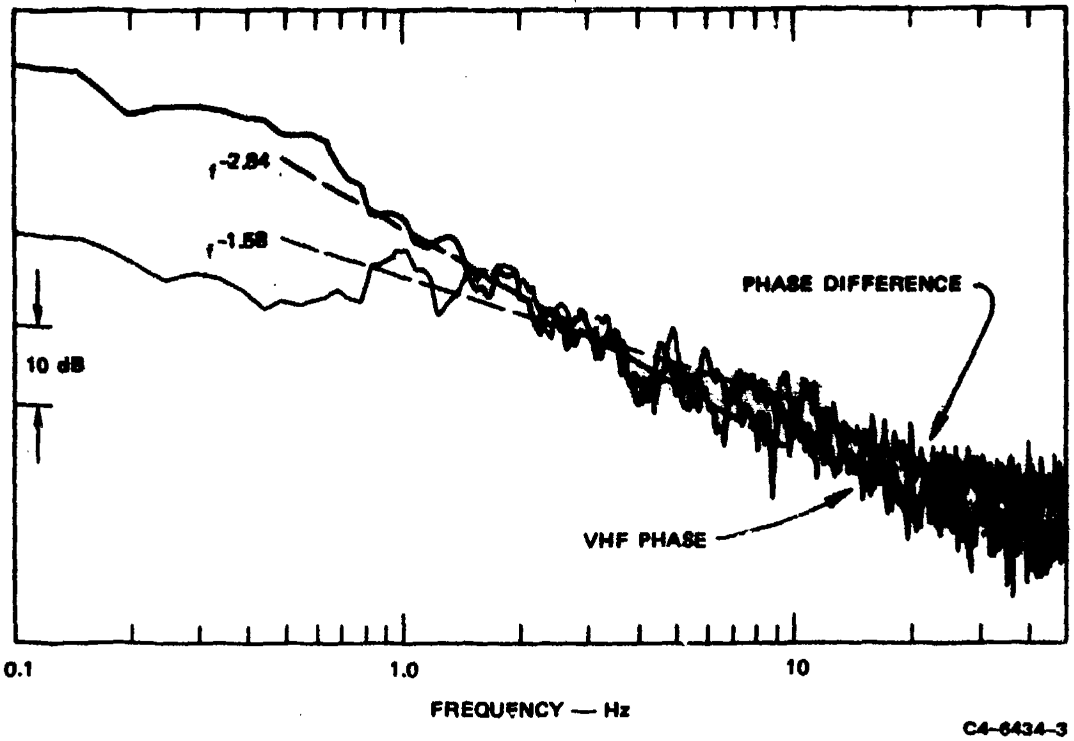

FIGURE 3 SPECTRAL DENSITY OF VHF PHASE AND VHF-UU3 PHASE DIFFERENCE FOR 20-s DATA RECORD FROM POKER FLAT PASS 6-36 AT ABOUT 0919 UT

We also conclude from Figure 3 that errors in T due to diffraction, which act to flatten the spectrum, are less severe than the corresponding errors in p. Strong scatter effects, which are evident in Figure 2(a) after 0920 UT, also generate mainly high-frequency components. Ultimately, strong-scatter effects will drive the phase spectrum toward f^{-2}. By careful processing and data interpretation, we can usually recognize and avoid erroneous T and p values.

III INTENSITY SCINTILLATION

In this section we shall develop the form of the S_4 scintillation index in the limit of an infinitely large outer-scale cutoff. This limit is well defined because Fresnel filtering suppresses the contribution of large-scale components. The results take a fairly simple analytic form that properly accounts for the propagation-angle dependence of the scintillation. In Rufenach's (1975) formulas, which retain an explicit dependence on the outer scale, the angle dependence is introduced in an ad hoc manner.

We shall characterize the amplitude scintillation by the second-order moments of intensity. However, under the assumed weak-scatter conditions, the amplitude and log-amplitude are simply related. For example, the scintillation index S_4, which is the normalized rms intensity, is twice the rms amplitude index. The intensity autocorrelation function corresponding to Eq. (2) is

$$R_I(\Delta\vec{\rho}_s) = 4r_e^2\lambda^2 \, L \sec^2 \theta \iint \Phi_{\Delta N_e}(\vec{\kappa}, -\tan \hat{a}_{k_T} \cdot \vec{\kappa})$$

$$\times \sin^2\left(h(\vec{\kappa})Z\right) \cos \, (\vec{\kappa} \cdot \Delta\vec{\rho}_s) \, \frac{d\vec{\kappa}}{(2\pi)^2} \tag{20}$$

where

$$h(\vec{\kappa}) = \kappa^2 - \tan^2 \theta(\hat{a}_{k_T} \cdot \kappa)^2 \tag{21}$$

and

$$Z = \frac{\lambda z \sec \theta}{4\pi} \tag{22}$$

The square of the S_4 scintillation index is derived from Eq. (20) by letting $\Delta\vec{\rho}_s = 0$. If we substitute Eqs. (5) and (6) into Eq. (20), use Eq. (7), and then change variables, we obtain the simpler expression

$$S_4^2 = 4r_e^2\lambda^2(L \sec\theta)\, ab\iint \frac{C_s}{[q_o^2 + (A'q_x^2 + B'q_xq_y + C'q_y^2)]^{\nu+1/2}}$$

$$\times \sin^2 [(q_x^2 + q_y^2)Z]\, \frac{dq_x}{2\pi}\, \frac{dq_y}{2\pi} \tag{23}$$

The coefficients A', B', and C' are related to A, B, and C by Eq. (51) in in Rino and Fremouw (1977) where it is shown that Eq. (23) is equivalent to the Briggs-Parkin formula as generalized by Singleton (1973) [see also Rufenach (1975) and Costa and Kelley (1976)].

As it stands, Eq. (23) cannot be evaluated analytically. Rufenach (1975) and Costa and Kelley (1976) have used a slightly modified form of Eq. (23), which can be evaluated when $\nu = 1.5$. However, from the discussion in Section I, it follows that for ionospheric scintillation, $Zq_o^2 \ll 1$. Thus, it is a good approximation to take

$$S_4^2 = 4r_e^2\lambda^2(L \sec\theta)\, C_s\, Z^{\nu-1/2}\iint \frac{ab \sin^2 (q^2)\, dq_xdq_y/(2\pi)^2}{(A'q_x^2 + B'q_xq_y + C'q_y^2)^{\nu+1/2}} \tag{24}$$

which is the limiting form of Eq. (23) as $q_o \to 0$. Hereafter, we shall denote the double integral in Eq. (24) by I.

To evaluate I, we first perform a rotation of coordinates to remove the q_xq_y term. The result is

$$I = \iint \frac{ab \sin^2 (q^2)\, dq_xdq_y/(2\pi)^2}{(A''q_x^2 + C''q_y^2)^{\nu + 1/2}} \tag{25}$$

where

$$A'' = \frac{1}{2}[A' + C' + D'] \tag{26a}$$

$$C'' = \frac{1}{2}[A' + C' + D'] \tag{26b}$$

and

$$D' = \sqrt{(A' - C')^2 + B'^2}\ . \tag{26c}$$

We note that $A'' \geq C''$.

Now, I is separable such that after a series of manipulations,

$$I = \frac{1}{\pi^2} \int_0^{\infty} q^{-2\nu} \sin^2 (q^2)\, dq \int_0^{\pi/2} \frac{ab\, d\phi}{[A'' - (A''-C'') \sin^2 \phi]^{\nu + 1/2}} . \tag{27}$$

The integral over q is well known for scattering by isotropic irregularities. The integral over ϕ properly accounts for the geometrical effects of anisotropic irregularities. In contrast, Rufenach (1975) introduced an ad hoc multiplicative geometrical factor to account for anisotropic irregularities. By evaluating the integral over q and substituting Eq. (27) into Eq. (24) we have

$$S_4^2 = 4r_e^2\lambda^2 (L \sec \theta)\, C_s Z^{\nu-1/2} \left[\frac{-\Gamma\left(\frac{1-2\nu}{2}\right) \cos\, [\pi(1-2\nu)/4]}{2\pi\, 2^{(5\, -\, 2\nu)/2}}\right] \mathcal{J} \tag{28}$$

where

$$\mathcal{J} = \frac{2\, ab}{\pi A''^{(\nu+1/2)}} \int_0^{\pi/2} \frac{d\phi}{\left[1 - \frac{A'' - C''}{A''} \sin^2 \phi\right]^{\nu + 1/2}} \tag{29}$$

The integral in Eq. (29) can be evaluated in terms of the hypergeometrical function ${}_2F_1(\alpha, \beta; \nu; z)$ (see Gradshteyn and Ryzhik, 1965; Formula 3.681). To avoid convergence problems when $A'' \gg C''$, however, we have applied the transformation

$${}_2F_1(\alpha,\beta;\nu;z) = (1-z)^{\nu-\alpha-\beta}\, {}_2F_1(\nu-\alpha,\ \nu-\beta,\ \nu;\ z) . \tag{30}$$

Making the appropriate substitutions, $\mathcal{J}$ can be evaluated as

$$\mathcal{J} = \frac{ab}{\sqrt{A''}\, C''^{\nu}}\, {}_2F_1\left(1/2 - \nu,\ 1/2,\ 1;\ \frac{A'' - C''}{A''}\right) \tag{31}$$

Now, $\lim_{z\to 1} {}_2F_1(1/2 - \nu,\ 1/2,\ 1;\ z) = \Gamma(\nu)/[\sqrt{\pi}\,\Gamma(\nu + 1/2)]$. By direct computation from Eq. (27) when $a \gg 1$, it can be shown that this limit is correct.

To summarize, Eqs. (26), (28), and (31) can be used to evaluate the scintillation index under conditions of weak scattering in terms of C_s, ν, Z, and the propagation geometry. We note that the wavelength dependence of S_4 implied by Eq. (28) is $S_4 \propto \lambda^{(\nu+1.5)/2}$. Thus, if $\nu = 1.5$, which corresponds to $\varphi(f) \propto f^{-3}$, $S_4 \propto \lambda^{1.5}$, the nominal wavelength dependence typically reported for ionospheric data.

By using Eq. (16), we can write Eq. (28) in the equivalent form

$$S_4^2 = 4TZ^{\nu-1/2}\ C(\nu)\ (\mathcal{G}/C)\ v_{eff}^{-(2\nu-1)} \tag{32}$$

where

$$C(\nu) = -\frac{\Gamma\left(\frac{1-2\nu}{2}\right)\cos\ [\pi(1-2\nu)/4]\ \Gamma(\nu+1/2)\ (2\pi)^{2\nu}}{\Gamma(\nu)\sqrt{\pi}\ 2^{(5\ -\ 2\nu)/2}}\ . \tag{33}$$

If we note that the units of T are radians squared per hertz raised to the $2\nu + 1$ power, it is easily verified that Eq. (32) is dimensionally consistent. We also see from Eq. (32) that for a <u>fixed</u> rms phase level, S_4 varies inversely with v_{eff}, which increases with increasing height. Thus, while the factor $Z^{\nu-1/2}$ acts to increase S_4 with increasing height, the decreasing factor $v_{eff}^{-(2\nu-1)}$ dominates and S_4 actually decreases. As we shall see, this effect is important in interpreting the Wideband satellite data.

IV APPLICATION TO WIDEBAND SATELLITE DATA

A. General

We shall now apply the phase-screen model to the interpretation of Wideband satellite data. As discussed in Fremouw et al. (1978), we routinely measure the phase SDF at VHF (137 MHz) and UHF (378.6 MHz). The spectral estimates are smoothed, after which a log-linear least-squares fit is applied to determine the spectral strength parameter T and the spectral index p. Thus, $\varphi_{\phi}(f) \approx Tf^{-p}$ over the significant portion of the phase SDF. The frequency limits for the fit are carefully chosen to minimize noise contamination and detrend filter effects.

We shall first apply Eq. (17) to compare the calculated and measured rms phase. If the two results agree, we can be confident that the phase SDF is indeed accurately modeled by the power-law form. Thus, this first step is mainly a consistency check for the basic parameters T and p.

The next step is to apply Eq. (32) to compute S_4 for comparison with its measured value. To evaluate Eq. (32), however, we must specify the height of the phase screen, z, the relative scan velocity, $\vec{v}$, and the anisotropy parameters a, b, δ, where a is the axial ratio along the magnetic field, b is the axial ratio transverse to the magnetic field, and δ is the orientation of the transverse axis such that $\delta = 0$ for geomagnetic east-west sheets (see Rino and Fremouw, 1977).

In our routine summary analysis we calculate the satellite component of the relative scan velocity and the propagation angles at two reference altitudes--namely, 110 km and 350 km. Thus, if the satellite component dominates the irregularity drifts we can compute S_4 at E- and F-region altitudes for different anisotropy parameters. When we achieve a good fit to the data, we can remove the geometrical factors in Eq. (16) to estimate the strength of turbulence times the layer thickness LC_s.

Because we have no direct means of determining the effective layer thickness, LC_s is the most basic measure of the irregularity strength. For display purposes, however, we shall specify a representative layer thickness from which an actual value for C_s can be obtained. The interpretation of C_s will be discussed in Section V.

B. Equatorial

Before considering individual passes, it is useful to look at the average behavior of the spectral index p. As we noted in Section II, the measured value of p is sensitive to noise contamination under conditions of weak scattering and to diffraction effects under conditions of strong scattering. To demonstrate these effects, we have plotted the average value of p versus S_4 for a representative set of passes.

The Ancon data are shown in Figure 4. The measured p index achieves a maximum value near but slightly less than 3 for S_4 values between 0.4 and 0.6. Noise contamination and diffraction effects cause the respective reductions of the measured p values for weak ($S_4 < 0.4$) and strong ($S_4 > 0.6$) fading levels. The wavelength dependence of S_4 under conditions of weak scattering provides an independent means of verifying the value of p.

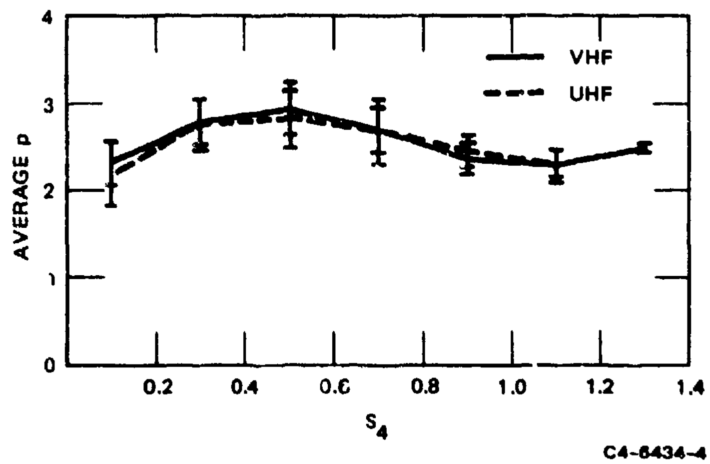

FIGURE 4 AVERAGE VALUE OF p FOR S_4 VALUES WITHIN THE INTERVALS $0.2\,n \leq S_4 < 0.2\,(n+1)$ AS DERIVED FROM ANCON DATA. The UHF and VHF curves are computed separately.

In Figure 5 we show a scatter diagram of Ancon S_4 values measured at VHF and UHF. The paucity of data between $S_4 = 0.2$ and $S_4 = 0.5$ is due to the tendency of the equatorial VHF scintillation to be either weak or strong (Livingston, 1978). In any case, the $\lambda^{1.5}$ curve, which corresponds to p = 3, fits the data quite well. The fit is more striking in Figure 6, where we have plotted S_4 at UHF against S_4 at L band.

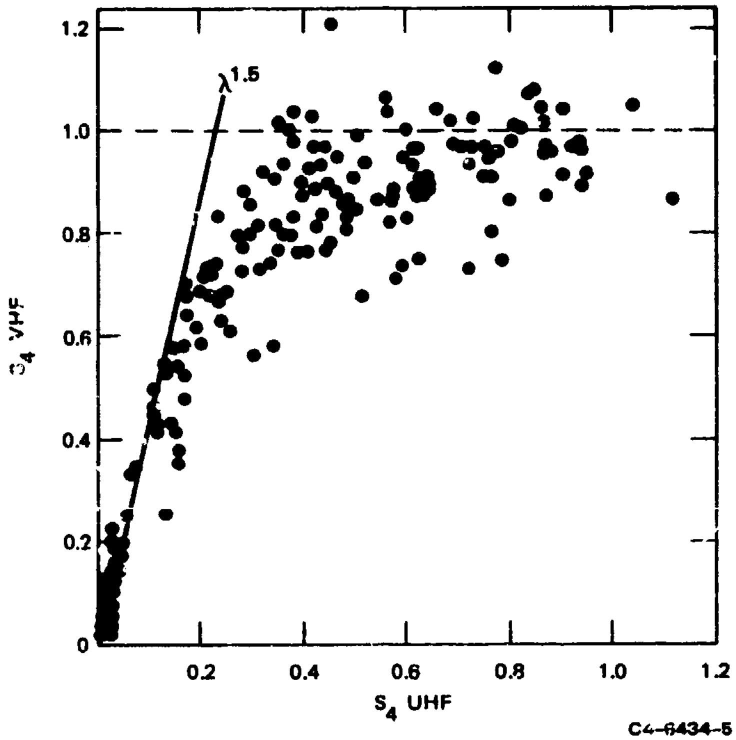

FIGURE 5 SCATTER DIAGRAM OF S_4 AT VHF vs S_4 AT UHF FOR A SUBSET OF THE ANCON PASSES USED IN GENERATING THE CURVES IN FIGURE 4

The average p values for the Kwajalein data show behavior similar to to that of the Ancon data (see Figure 7). However, the maximum average p value falls distinctly below p = 3. The corresponding shallower wavelength dependence of S_4 is consistent with a smaller p index as shown in Figures 8 and 9 where we have plotted the S_4 scatter diagrams for VHF versus UHF, and UHF versus L band. Thus, it appears that the phase spectra obtained from the Kwajalein data are systematically flatter than the phase spectra obtained from the Ancon data.

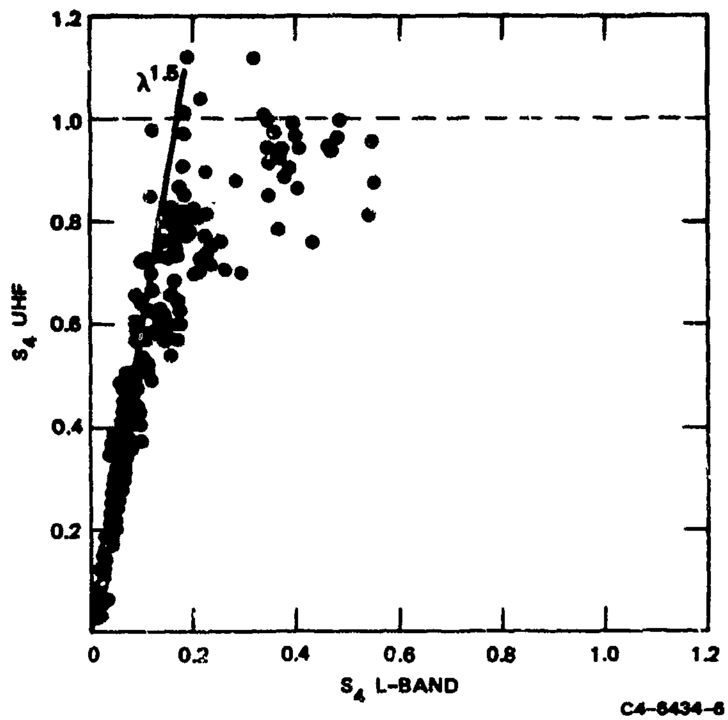

FIGURE 6 SCATTER DIAGRAM OF S_4 AT UHF vs S_4 AT L-BAND FOR A SUBSET OF THE ANCON PASSES USED IN GENERATING THE CURVES IN FIGURE 4

In both the Ancon data (Figures 5 and 6) and the Kwajalein data (Figures 8 and 9) saturation of the intensity scintillation apparently occurs for an S_4 value less than unity. (An S_4 value of unity corresponds to Rayleigh fading.) This effect is due to our detrending operation, which is applied separately to intensity and phase. The strong fading data from the equatorial stations evidently contained significant Fourier components beyond the 10 s cutoff of the detrend filter. This will not be a problem for our analysis here because we are considering only weak-scatter data in this report.

In Figure 10 we show the phase and intensity scintillation data for a disturbed nighttime Ancon Wideband pass together with a set of theoretical calculations of S_4 and σ_ϕ. Consider first the rms phase. We see that $\nu = 1.3$ gives as good a fit to the data as the $\nu = 1.5$ curve, which corresponds to an f^{-3} phase SDF. As we have already noted, diffraction

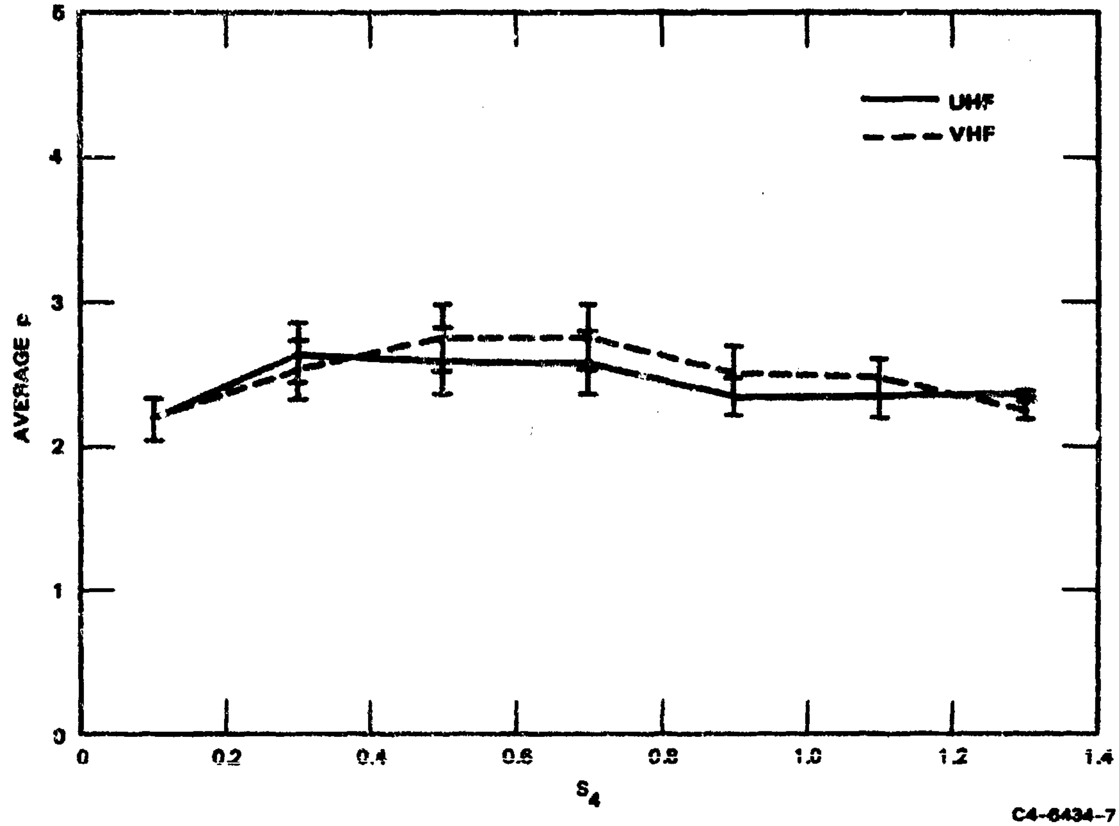

FIGURE 7 AVERAGE VALUES OF p FOR S_4 VALUES WITHIN THE INTERVALS $0.2\,n \leq S_4 < 0.2(n+1)$ AS DERIVED FROM KWAJALEIN DATA

effects cause a flattening of the phase SDF, which explains the discrepancy between the measured and calculated rms phase after ~ 0345 UT.

The F-region S_4 curve in Figure 10 for $\nu = 1.3$ comes closer to the measured S_4 curve than the corresponding $\nu = 1.5$ curve. However, in the regime where S_4 is small and we expect the weak-scatter theory to be applicable, the theoretical curve gives a result that is consistently too large. As we noted at the end of Section III, however, raising the equivalent phase screen height lowers S_4 for a specified rms phase level.

Thus, we believe that the S_4 discrepancy in Figure 10 is due to the 350-km reference altitude being too low. Unfortunately, the propagation angles are only computed for two heights. Nonetheless, in

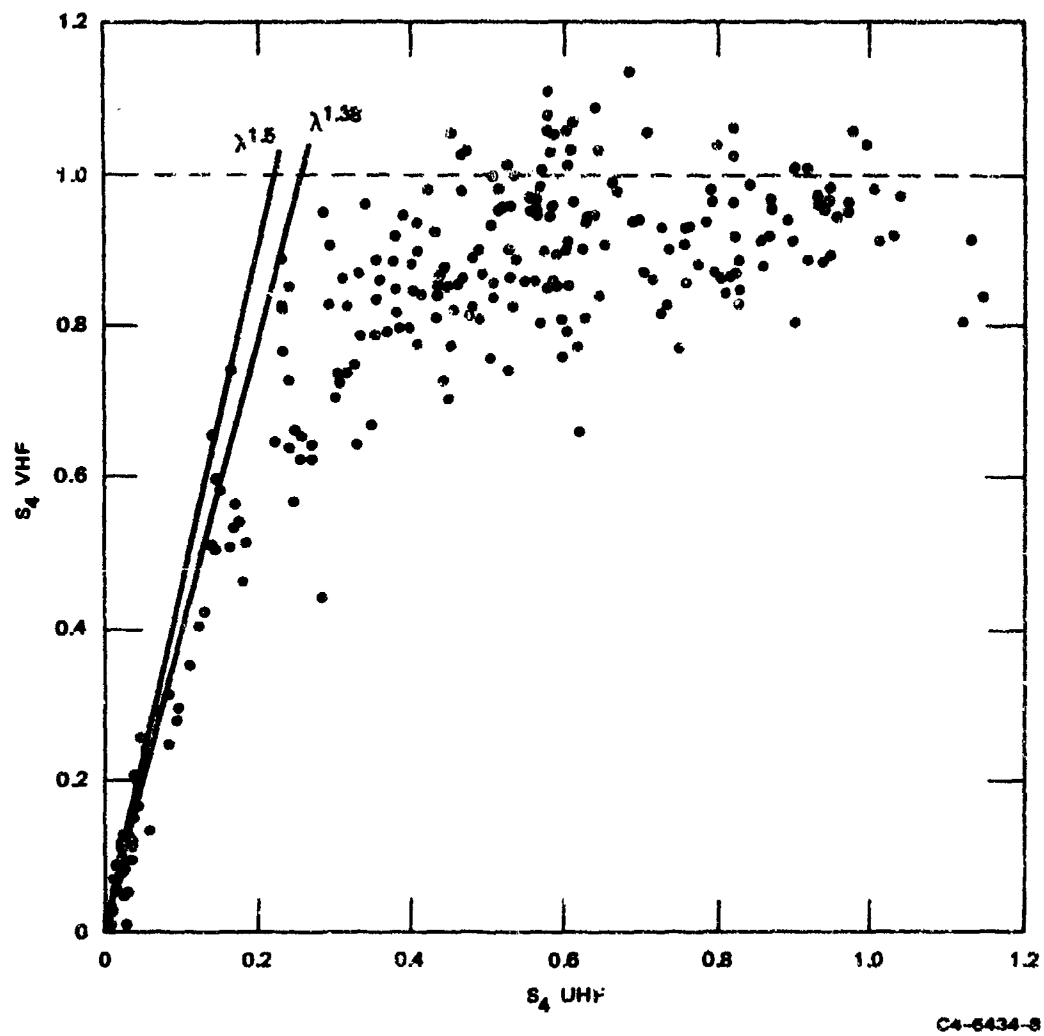

FIGURE 8 SCATTER DIAGRAM OF S_4 AT VHF vs S_4 AT UHF FOR A SUBSET OF THE KWAJALEIN PASSES USED IN GENERATING THE CURVES IN FIGURE 7

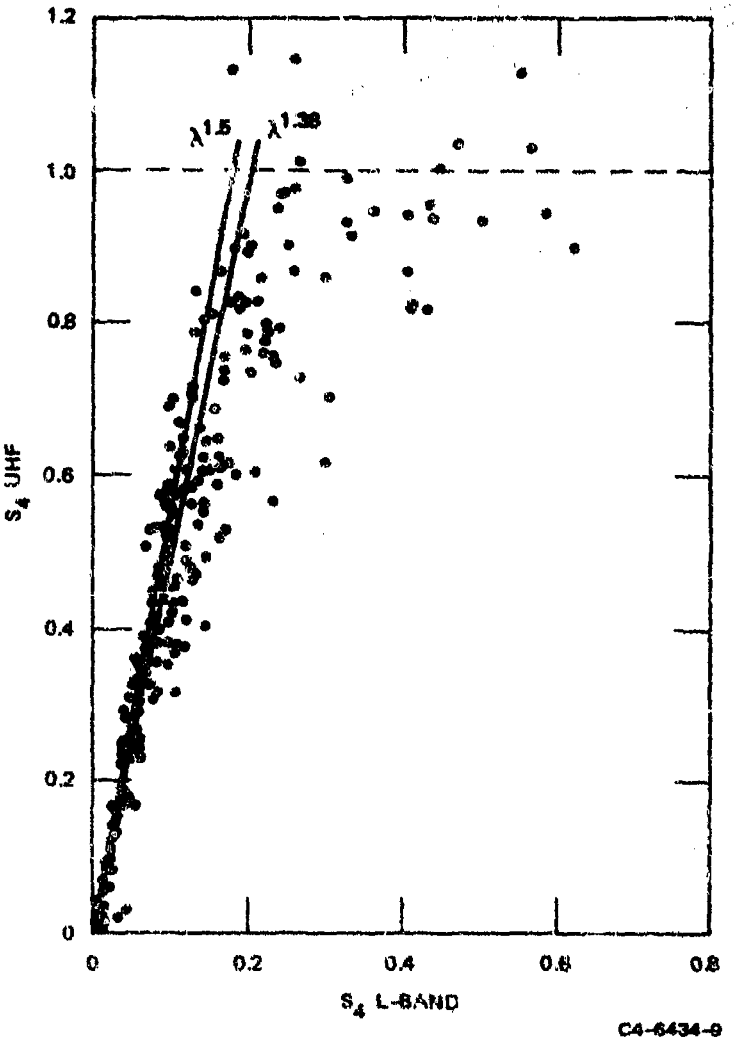

FIGURE 9 SCATTER DIAGRAM OF S_4 AT UHF vs S_4 AT L-BAND FOR A SUBSET OF THE KWAJALEIN PASSES USED IN GENERATING THE CURVES IN FIGURE 7

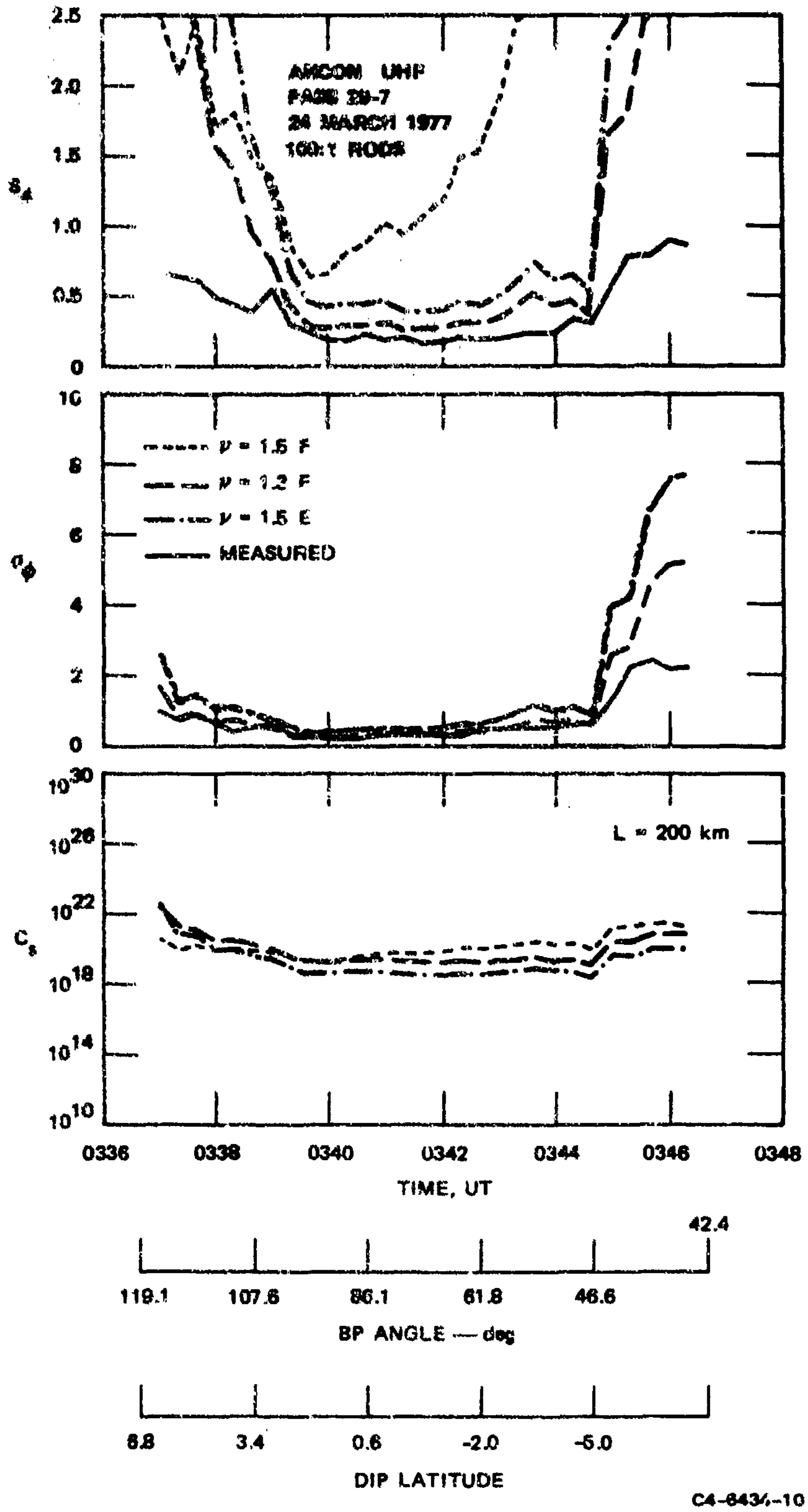

FIGURE 10 UHF DATA FROM ANCON PASS 29-7

Figure 10 we show the calculations for the E-region reference altitude. Again, the large S_4 estimates for the E-region are due to the smaller scan velocities [see Eq. (32)]. Finally, the large overestimates of S_4 when S_4 is greater than ~ 0.4 are due to the fact that the weak-scatter theory does not allow for multiple scattering.

To illustrate the axial-ratio dependence of S_4 we have used the geometry for Ancon Pass 29-7, but have assigned a fixed value to C_s. The corresponding S_4 values for isotropic irregularities and axial ratios of 5:1 and 100:1 are shown in Figure 11. Both the variation of S_4 with changing propagation geometry and the magnitude of S_4 decrease with increasing axial ratio until the axial ratio exceeds 10:1. Beyond 10:1, the S_4 index for the equatorial geometry does not exhibit an axial ratio dependence. The diffraction is then effectively two-dimensional, as discussed in Section III.

To complete the equatorial examples from Ancon, we have selected three additional passes and applied the nominal F-region geometry with $\nu = 1.4$ and a 100:1 axial ratio. The results are shown in Figures 12, 13, and 14. In Figure 12, the calculated S_4 values fall slightly below the measured values. For such low S_4 values, noise contamination is a possible explanation (see Appendix). However, increasing the ν value and/or lowering the reference altitude will tend to increase the model values as we have noted.

In Figure 13, the measured S_4 values are significantly larger than those shown in Figure 12. Thus, we expect the model calculations to overestimate S_4. There is a general tendency for the measured phase to fall below the theoretical curve, which is evidently the diffraction effect we have already noted. Nonetheless, the C_s values should be roughly correct, and indicative of the turbulence levels required to produce significant gigahertz scintillation. The data set shown in Figure 14 falls between the extremes shown in Figure 12 and 13. The overall fit in Figure 14 is quite good.

Turning now to the Kwajalein data, in Figure 15 we show a typical disturbed nighttime pass. The rms phase calculations for $\nu = 1.25$ clearly

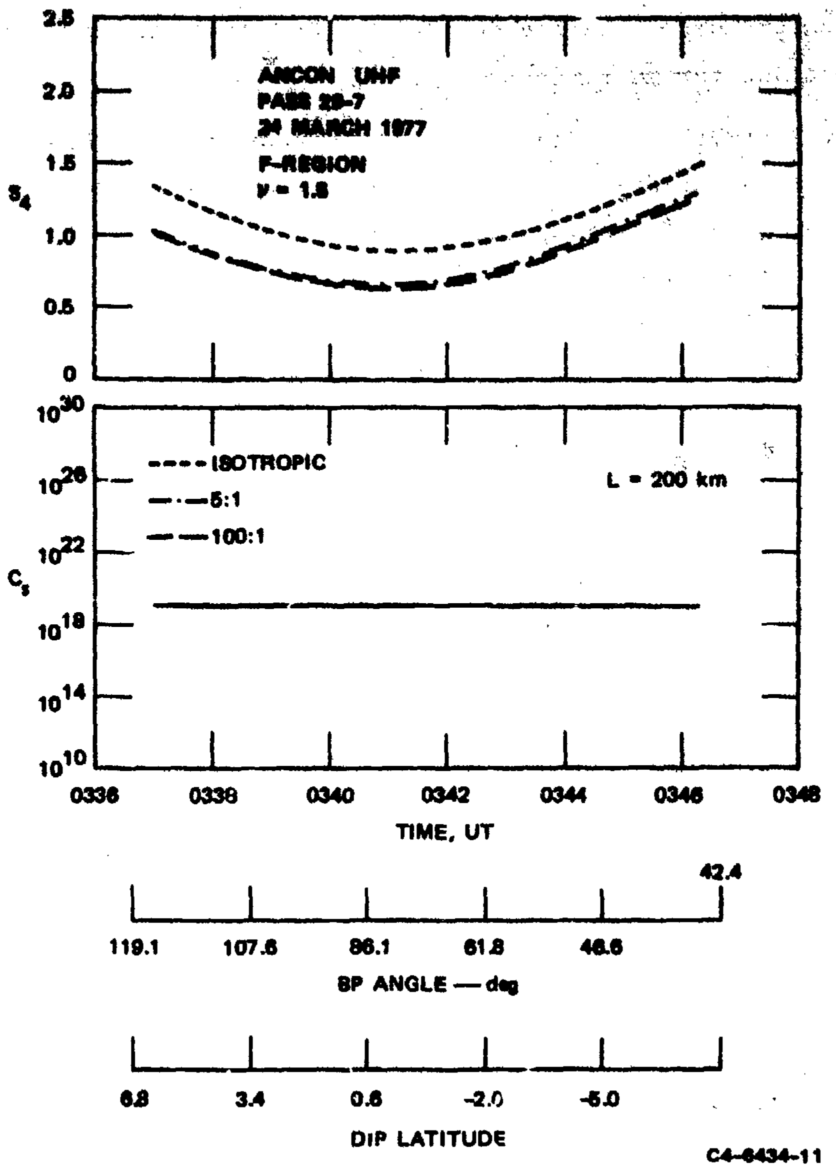

FIGURE 11 VARIATION OF S_4 AND FOR FIXED STRENGTH OF TURBULENCE SHOWING EFFECT OF CHANGING AXIAL RATIO

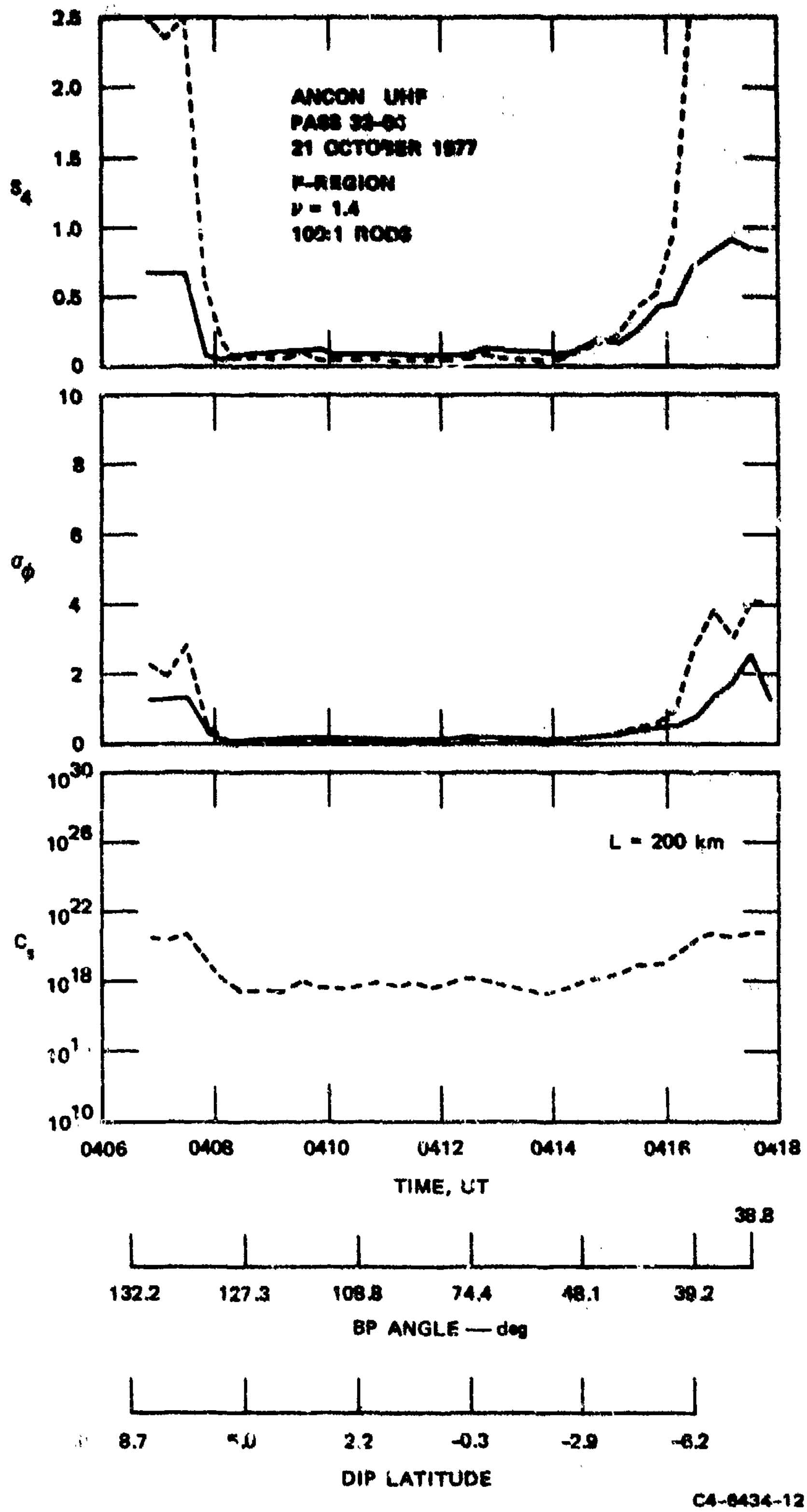

FIGURE 12 UHF DATA FROM ANCON PASS 32-04

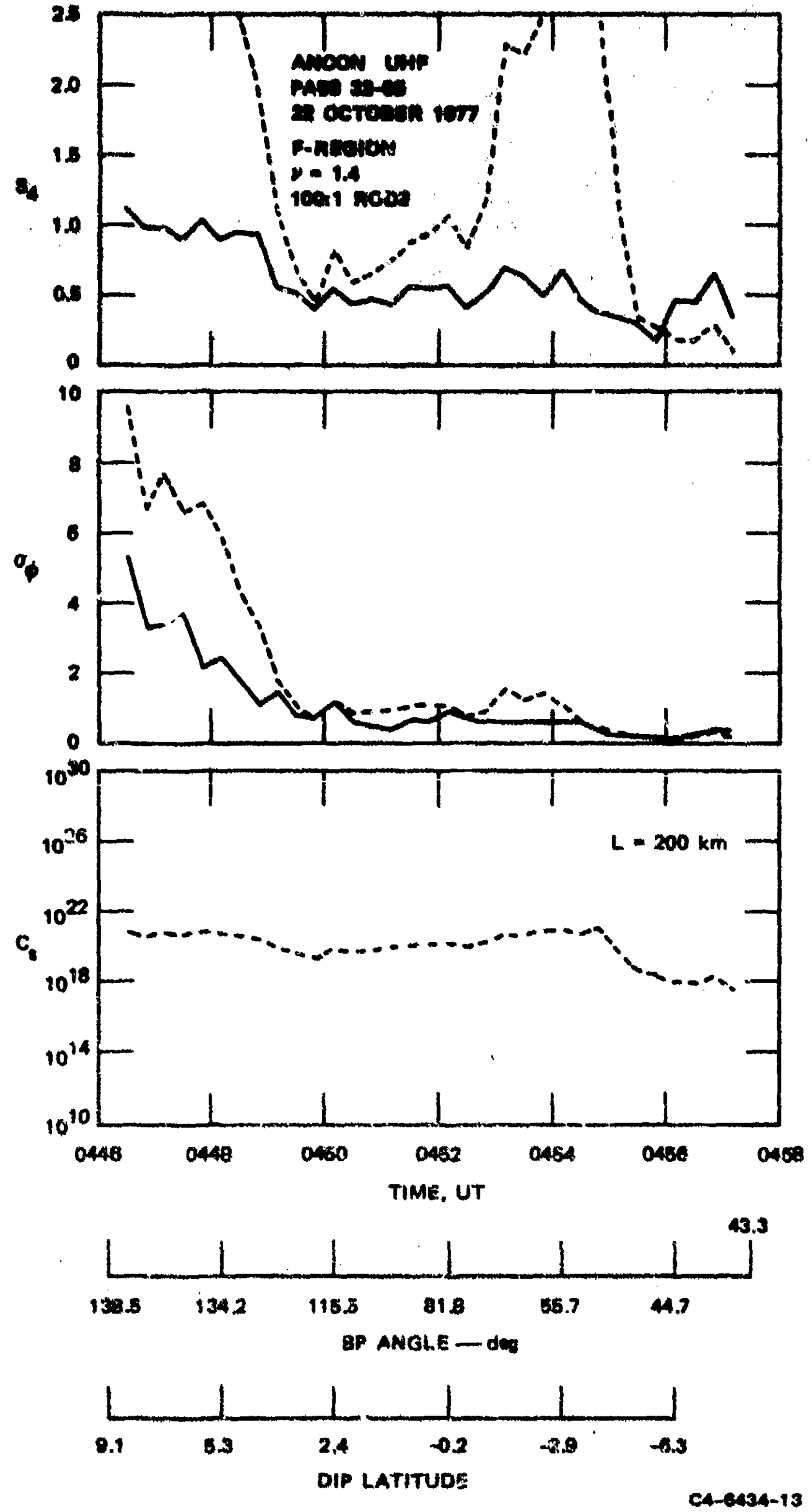

FIGURE 13 UHF DATA FROM ANCON PASS 32-05

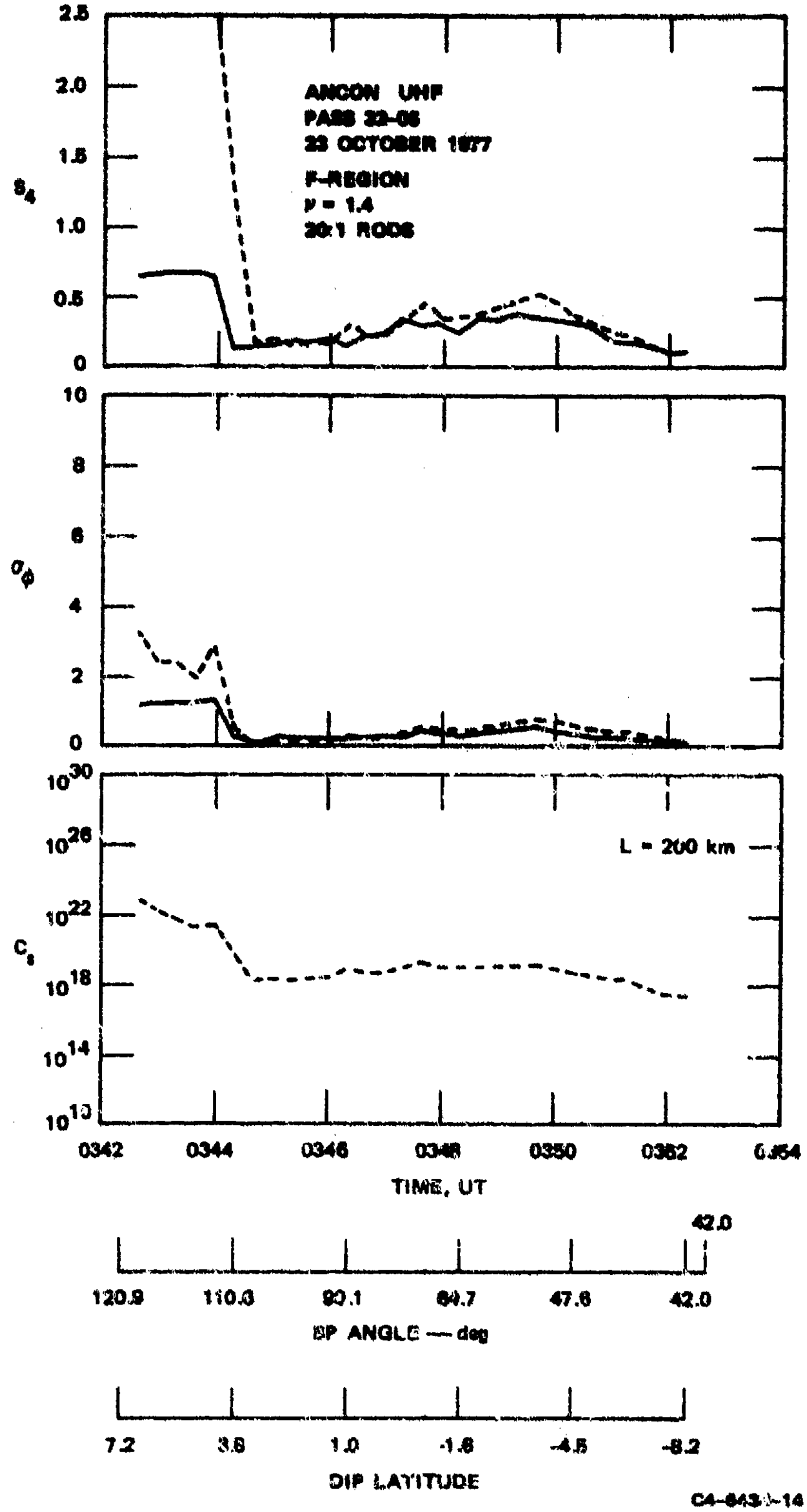

FIGURE 14 UHF DATA FROM ANCON PASS 2?-06

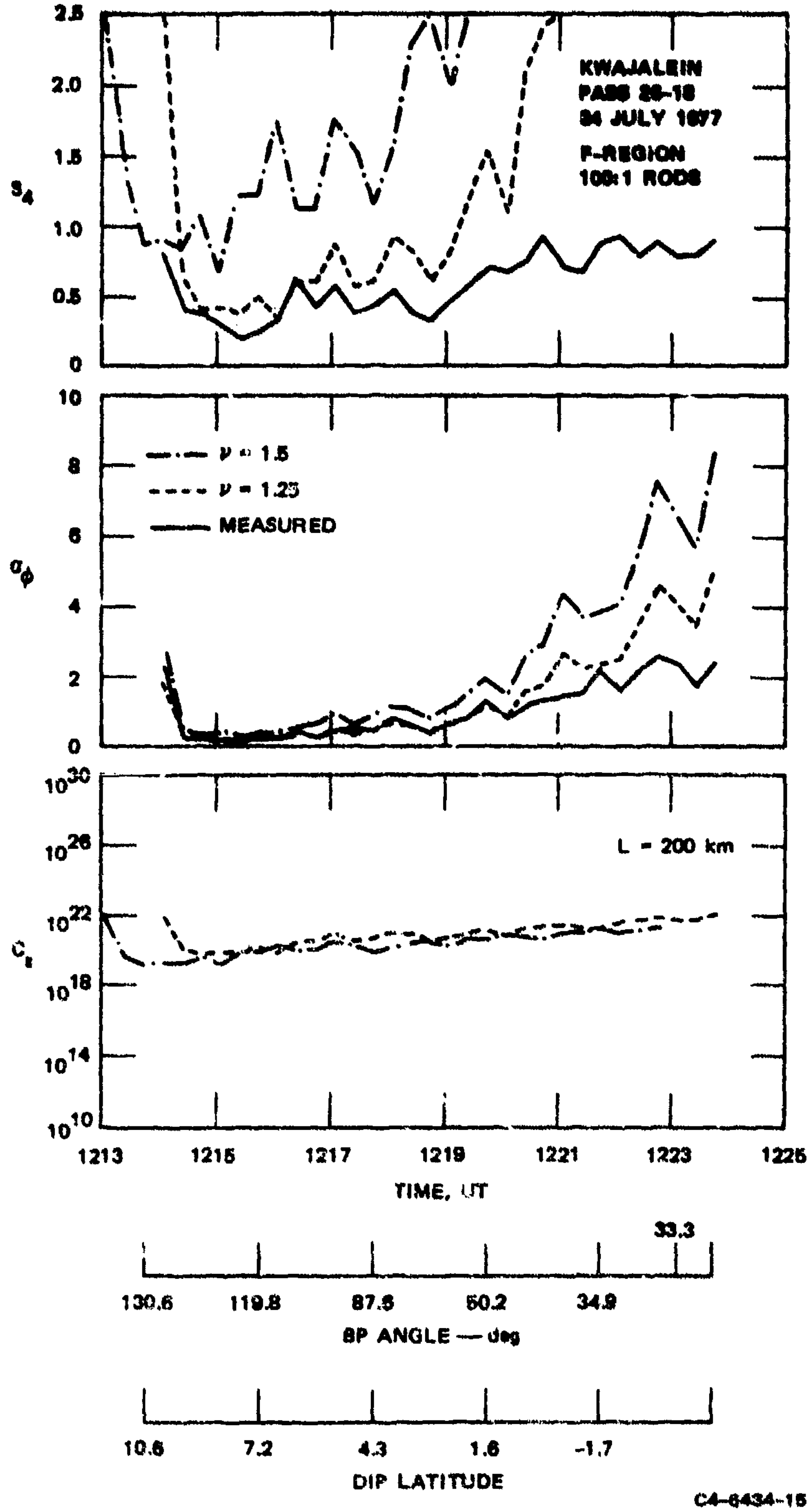

FIGURE 15 UHF DATA FROM KWAJALEIN PASS 26-18

fit the rms phase data better than the calculations using $\nu = 1.5$. As with the Ancon data, however, there is a tendency for the F-region S_4 curve to slightly overestimate the data which we have attributed to increased layer height. Thus, the only systematic difference between the Ancon and Kwajalein data that can be ascertained from the first-order moments is the lower phase spectral index--$p \sim 2.5$ for Kwajalein versus $p \sim 2.8$ for Ancon. This difference implies somewhat sharper phase gradients in the Kwajalein data than in the Ancon data.

As a final comment on the equator data, we have not made direct computations at L-band because the L-band phase data are not routinely Fourier analyzed. On the other hand, we have verified the wavelength dependence of S_4 between UHF and L-band in Figures 6 and 9. Moreover, even if UHF is near saturation, the phase scintillation and/or T can be frequency scaled with a high degree of accuracy. Thus, the self-consistent intensity and phase calculations at UHF can be accurately extrapolated to L-band. An example is presented in Section V.

C. Auroral

The interpretation of the auroral-zone data is complicated by the rapidly changing propagation geometry. Moreover, auroral-zone scintillations are typically associated with extreme variations in perturbation strength, albeit at substantially smaller levels than the equatorial data. As with the equator data, we begin by considering the general behavior of the spectral index.

A plot of p versus S_4 for a representative sampling of Poker Flat passes is shown in Figure 16. Here the average spectral index obtained from the VHF phase spectra is less than 2.5. A set of disturbed passes were used to obtain the UHF values, which tend to give a slightly larger p index. Thus, there may be a systematic steepening of the auroral phase spectra with increasing perturbation strength, or associated with those events that produce significant UHF scintillation.

In general, it appears that the auroral data tend to show even steeper phase gradients than the equatorial data from Kwajalein.

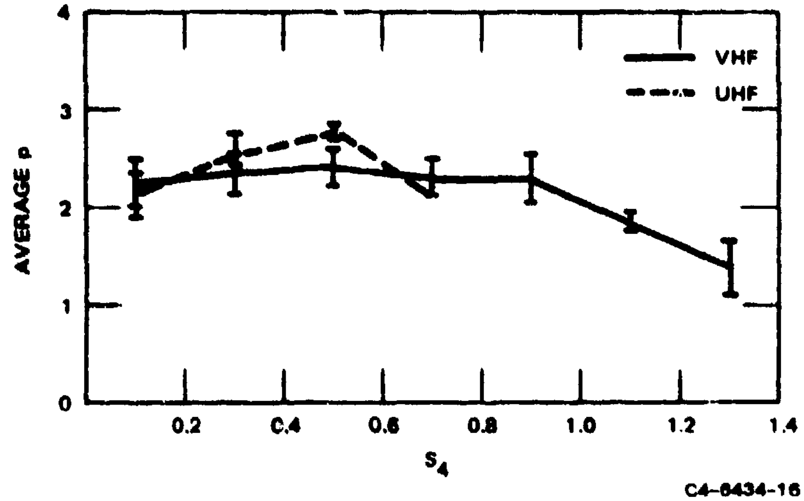

FIGURE 16 AVERAGE VALUE OF p vs S_4 AS IN FIGURES 4 AND 7. The VHF data are derived from 50 representative Poker Flat passes. The UHF data are derived from four disturbed Poker Flat passes.

However, the auroral data have shown considerably more variability in the measured p index and the overall structure of the scintillation. This is evident in the scatter diagram of S_4 values at UHF versus S_4 values at VHF shown in Figure 17. The $\lambda^{1.25}$ curve corresponds to a p index value of 2, which is more typical of reported in-situ measurements than phase scintillation measurements.

As a first detailed example of auroral-zone data, we have selected a nearly overhead pass with an isolated scintillation enhancement near the point of closest approach to the magnetic zenith. Such events are commonly observed under conditions of moderate auroral activity. The pattern of these events in passes to the east and west of the station is such that they tend to occur where the propagation path lies within the local L-shell. Thus, we have hypothesized a sheet-like anisotropy for the irregularities.

In Figure 18 we show the data and theoretical calculations for east-west-aligned sheets with a = b = 10 (10:10:1 notationally) at E- and F-region reference altitudes. The rms phase calculation using ν = 1.25 fits the data very well except near the localized enhancement. Here the

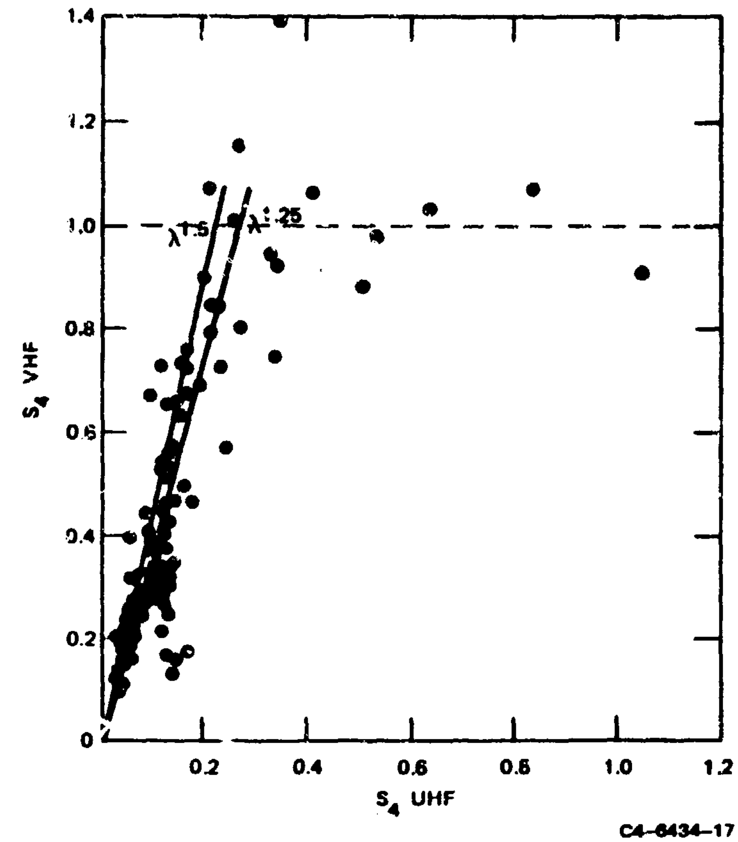

FIGURE 17 SCATTER DIAGRAM OF S_4 MEASURED AT VHF vs S_4 MEASURED AT UHF FOR THE FOUR DISTURBED PASSES USED IN GENERATING THE UHF CURVE IN FIGURE 16

phase SDF steepens such that p = 3. We believe this effect is due to the nonstationarity induced by the rapidly changing propagation geometry. Indeed, a purely geometrical effect should produce no change in the spectral shape.

The E-region and F-region S_4 curves for 10:10:1 sheets tend to bracket the data near the enhancement. Hence, if the 10:10:1 sheet model is correct, the equivalent phase screen must be placed between the E- and F-region reference altitudes. We note, however, that both calculations underestimate the measured S_4 values at the extremes of the pass. Rod-like irregularities, however, fit the data quite well.

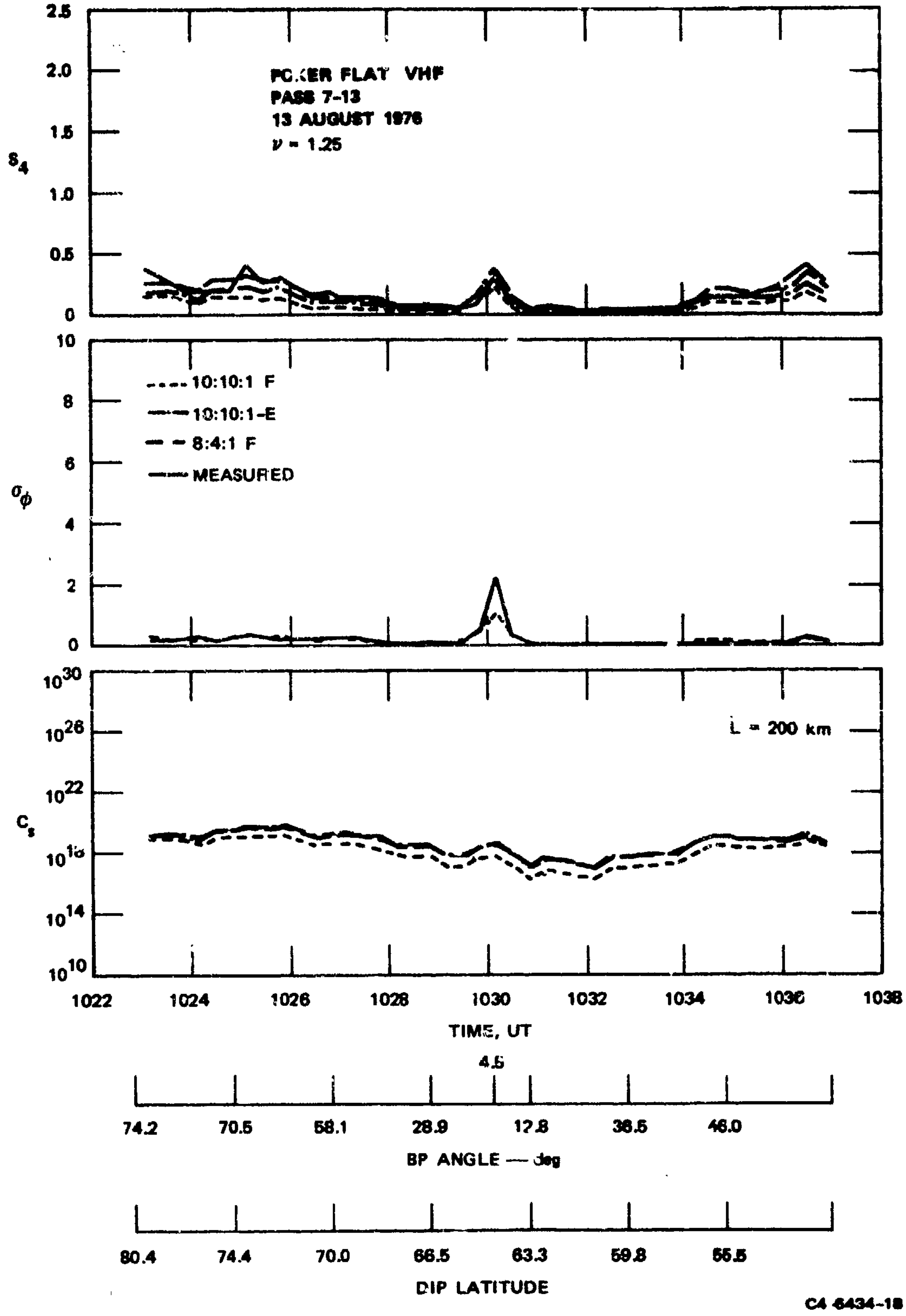

FIGURE 18 VHF DATA FROM POKER FLAT PASS 7-13 SHOWING ISOLATED SCINTILLATION ENHANCEMENT ATTRIBUTED TO GEOMETRY

We have hypothesized that the sheet-like structures, which are independently verified by analysis of the Wideband spaced-receiver data (Rino and Livingston, 1978), are confined to the region of the diffuse (continuous) and discrete aurora. Outside these precipitation regions, the irregularity structures are more nearly rod-like. To illustrate this possibility, we also show the theoretical curve for 8:4:1 sheets in Figure 18. The 8:4:1 curve underestimates the enhancement, but fits the extremes quite well.

Now, it has been noted from the earliest Wideband data (Fremouw et al., 1978) that the auroral-zone data show a large number of events in which the phase scintillation level is much larger than the corresponding intensity scintillation level, even though the latter remains in the weak-scatter regime. The geometrical enhancement produces such an effect. The rms-phase-to-S_4 ratio at the rms phase peak for the data in Figure 18 approaches 4.0. We shall see, however, that there are other events that produce large rms phase enhancements without a proportionate enhancement in S_4.

In Figure 19 we show an example of a disturbed low-elevation pass. The rms phase data fit the $\nu = 1.25$ curve better than the $\nu = 1.5$ curve. Near 0912 UT, diffraction effects tend to reduce the measured rms phase below the predicted value just as in the equator data. The predicted S_4 values for the F-region 10:10:1 sheet model fit the measured data very well in the region between 0909 UT and 0911 UT. Before 0909, however, the theoretical F-region calculations underestimate the measured values of S_4 and the E-region calculations give a better fit. For completeness, we also show the $\nu = 1.5$ F-region curve, which clearly gives a poorer fit to the measured S_4 curve as well as to the rms phase data.

The change in structure that occurs at 0909 UT is evidently due to an increase in height of the corresponding irregularities. Recall that for a given phase scintillation level, the self-consistent S_4 value decreases with increasing height, and vice versa. This implies that increasing the layer height tends to enhance the ratio of phase to amplitude scintillation. Unlike the geometrical enhancement, however, a

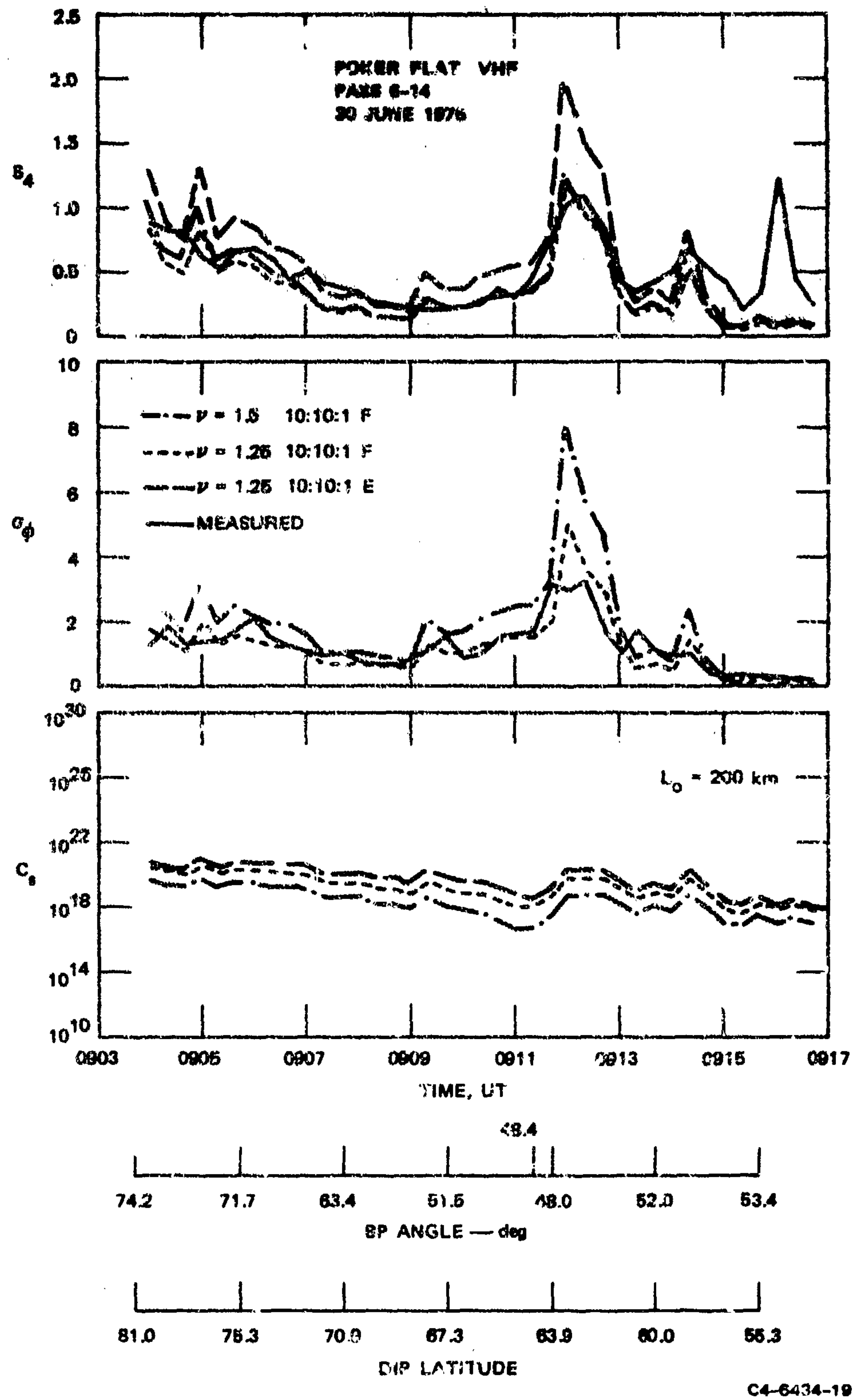

FIGURE 19 VHF DATA FROM POKER FLAT PASS 6-14 SHOWING EVIDENCE OF IRREGULARITY HEIGHT CHANGE

change in irregularity height would produce a roughly equivalent increase in the equatorial and auroral data. We noted one such event in Figure 10.

In Figure 20 we show another example of a high-elevation pass, but with a strong perturbation present. With the exception of the regions of large S_4 values, the F-region calculations with $\nu = 1.25$ and $\nu = 1.5$ fit the data reasonably well. However, between 1052 and 1054 UT the $\nu = 1.25$ curve underestimates the rms phase while the $\nu = 1.5$ curve overestimates the rms phase. Allowing for diffraction effects, there is evidence here of a systematic change in the phase spectrum within the pass.

In Figure 21 we show a more severe example of such an effect. We see that the rms phase enhancements are badly underestimated by the theoretical calculations, particularly between 0948 UT and 0952 UT. We believe that this is due to rapidly changing perturbation structures that do not readily admit a homogeneous spectral representation, rather than to some fundamental change in irregularity development leading a non-power-law spectral distribution. Either way, the effect is to produce large phase excursions without a proportionate increase in S_4.

Such events are not uncommon in the auroral data. However, while they are not properly characterized using signal moments calculated under the weak-scatter theory, the measured anisotropy and relative pattern drifts obtained from the spaced receiver data are well behaved (see Rino and Livingston, 1978). It is from such an analysis that the E-region model with a = 8 and b = 4 in Figure 21 was deduced. It is interesting that in spite of the poor fit to the rms phase data, the E-region model calculations fit the S_4 data reasonably well.

To summarize the auroral data, we have shown that as long as the rms phase data fit the power-law model and S_4 is less than 0.4, the weak-scatter power-law phase-screen model gives self-consistent results for rms phase and intensity with an appropriate choice of irregularity (phase-screen) height and irregularity anisotropy. Indeed, the model is particularly sensitive to irregularity height and detailed anisotropy.

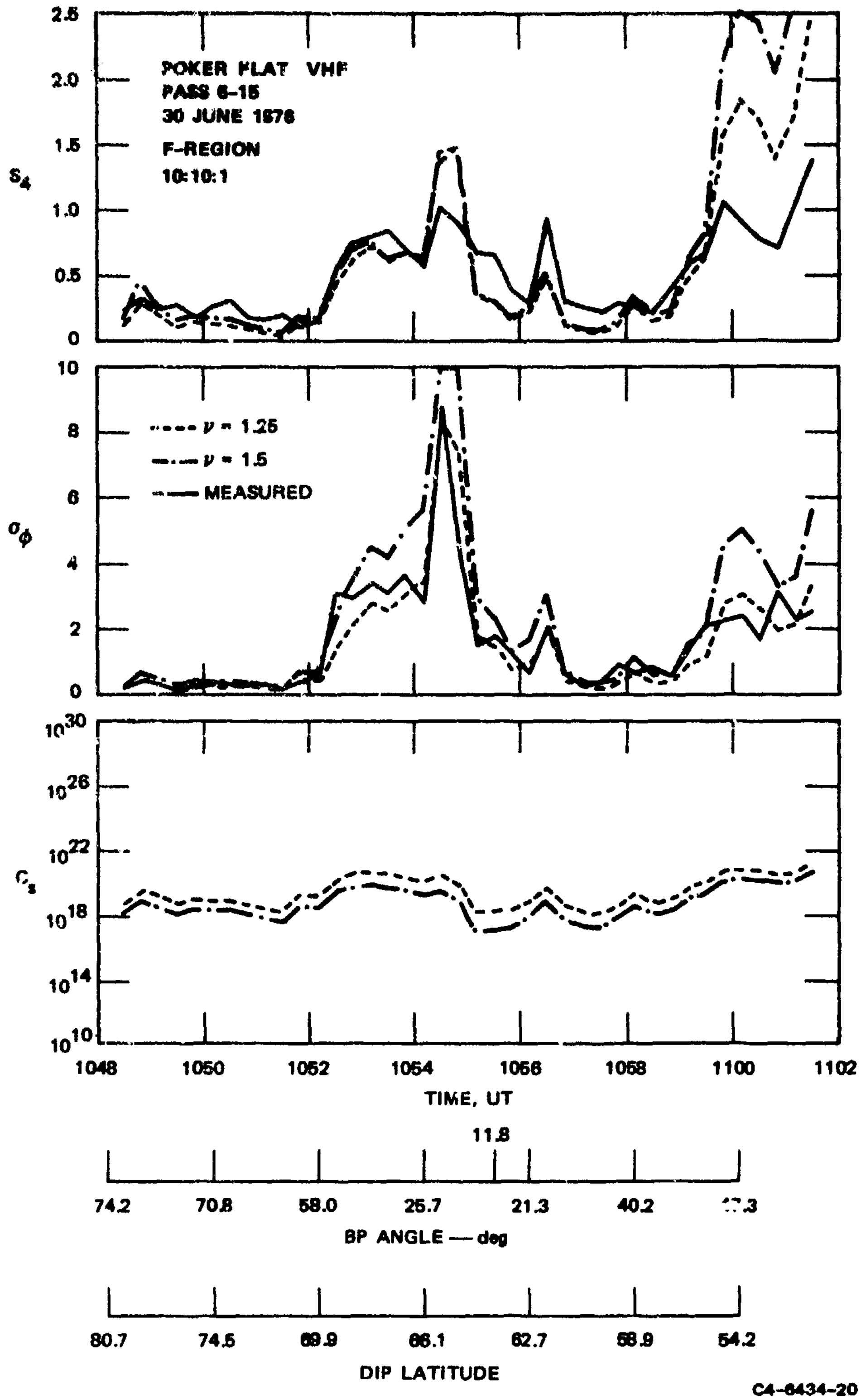

FIGURE 20 VHF DATA FROM POKER FLAT PASS 6-15 SHOWING EVIDENCE OF CHANGE IN PHASE SPECTRA

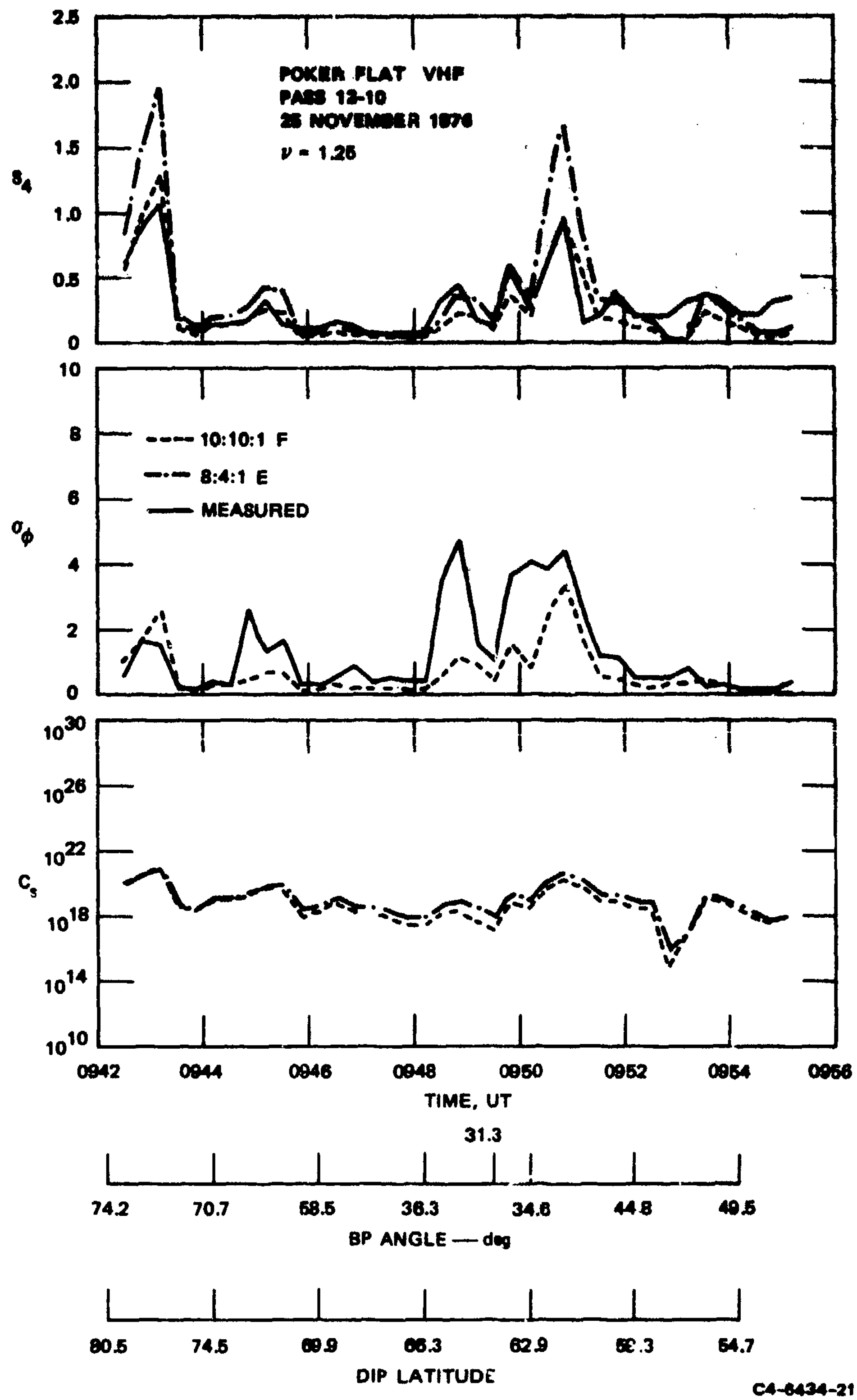

FIGURE 21 VHF DATA FROM POKER FLAT PASS 12-10 SHOWING EVIDENCE OF NON-POWER-LAW PHASE STRUCTURES

We have taken F-region irregularities with a 10:10:1 sheet-like anisotropy as representative of auroral-zone irregularities. However, we have not attempted to demonstrate unequivocally here that the sheet model, as opposed to a simple rod-like anisotropy, is correct. A separate report will address the irregularity anisotropy in detail. A point to be made here, however, is that wherever a localized geometrical enhancement occurs, the rms phase increases more rapidly than the increase in S_4.

We have also shown non-geometry-associated events that produce large rms phase enhancements without a proportionate S_4 increase. Such events show pronounced departures from the simple power-law model we have employed in our analysis. Hence, the theory is inappropriate in such cases. We believe that such events are representative of undeveloped turbulence. A smooth auroral arc is representative of a structure that can produce large localized phase enhancements without a proportionate increase in S_4. It is clear that such structures are not appropriately characterized by second-order moments.

V DISCUSSION

In this report we have first developed rms phase and S_4 formulas based on a power-law-phase-screen model with an arbitrarily large outer-scale cutoff. The formulas allow fully for the angle dependence of the signal moments in a highly anisotropic medium. We have shown that the power-law-phase-screen model gives an accurate self-consistent description of the phase and intensity scintillation under conditions of weak ($S_4 \leq 0.4$) intensity scintillation.

The height of the equivalent phase screen and the anisotropy of the irregularity are the only free parameters in the theory. We have found that the parameter sensitivity of the model is such that reasonable bounds can be put on the height and anisotropy. We have not, however, tried to carefully determine the morphology of the irregularity height here because this can be better accomplished by using the interferometer data. That analysis is being reported separately (Rino and Livingston, 1978).

Our main purpose in presenting the analysis in this report is to demonstrate the adequacy of the phase-screen model for translating the routinely measured Wideband summary parameters to invariant irregularity strength measures. Such translations are necessary, for example, to predict phase perturbation levels that might adversely affect advanced surveillance satellite systems. They also enable us to predict intensity scintillation, particularly the equatorial gigahertz scintillation that can adversely affect satellite communication systems.

To demonstrate how the model can be used, let us consider a phase screen at 350 km with a signal source at three times this height directly overhead at the geomagnetic equator. We can then use Eq. (27) to predict S_4 as a function of C_s. Since we have used 200 km for the layer thickness in deriving representative C_s values from our data, we shall also apply that value here. For illustrative purposes, we have used isotropic irregularities and 100:1 rods. Thus, in Figure 22(a) we have plotted S_4 curves at 1 GHz versus C_s for $\nu = 1.25$ and the corresponding curves in Figure 22(b) for $\nu = 1.5$. We see that C_s levels approaching 10^{22} correspond to significant levels of gigahertz scintillation.

Our entire analysis is based on the assumption that the three-dimensional irregularity SDF has the form $C_s/[q_o^2 + q^2]^{\nu+0.5}$. The corresponding spatial correlation function has the form

$$R_{\Delta N_e}(y) = \frac{C_s}{4\pi^{3/2}\,\Gamma(\nu + 1/2)} \left|\frac{2q_o}{y}\right|^{-\nu+1} K_{\nu-1}(q_o y) \quad . \tag{34}$$

It is easily shown that $\langle\Delta N_e^2\rangle$ as determined by evaluating $\lim_{y\to 0} R_{\Delta N_e}(y)$ is consistent with Eq. (7).

Now, if an in-situ probe scans the medium, the spectral density function that characterizes the probe output is obtained by Fourier transforming Eq. (34) with y replaced by $v_I\delta t$, where v_I is the effective probe velocity analogous to Eq. (12). The resulting SDF is

$$\varphi_p(f) = \frac{C_s\,\Gamma(\nu-1/2)}{4\pi^2\Gamma(\nu+1/2)}\,\frac{1}{v_I[q_o^2 + (2\pi f/v_I)^2]^{\nu-1/2}} \quad . \tag{35}$$

When $2\pi f/v_I \gg q_o$, $\varphi_p(f) = T_I f^{2\nu-1}$. Thus, if $\nu = 1.5$, the in-situ SDF varies as f^{-2}.

To determine C_s from $\varphi_p(f)$, one must know the anisotropy of the irregularities and the probe velocity. Moreover, the rms electron density is subject to the same ambiguity as the rms phase. However, if we assume that $q_o \doteq 2\pi/\ell_o$, where ℓ_o is the effective length of data interval used in estimating $\varphi_p(f)$, then Eq. (7) can be used to get some idea of the actual density perturbation levels involved.

In Figure 23 we show the rms electron density versus C_s for data intervals varying logarithmically from 1 km to 1000 km. We see that even for the 200-km layer we used for reference, the corresponding gigahertz C_s level of 10^{22} gives rise to rms electron density excursions

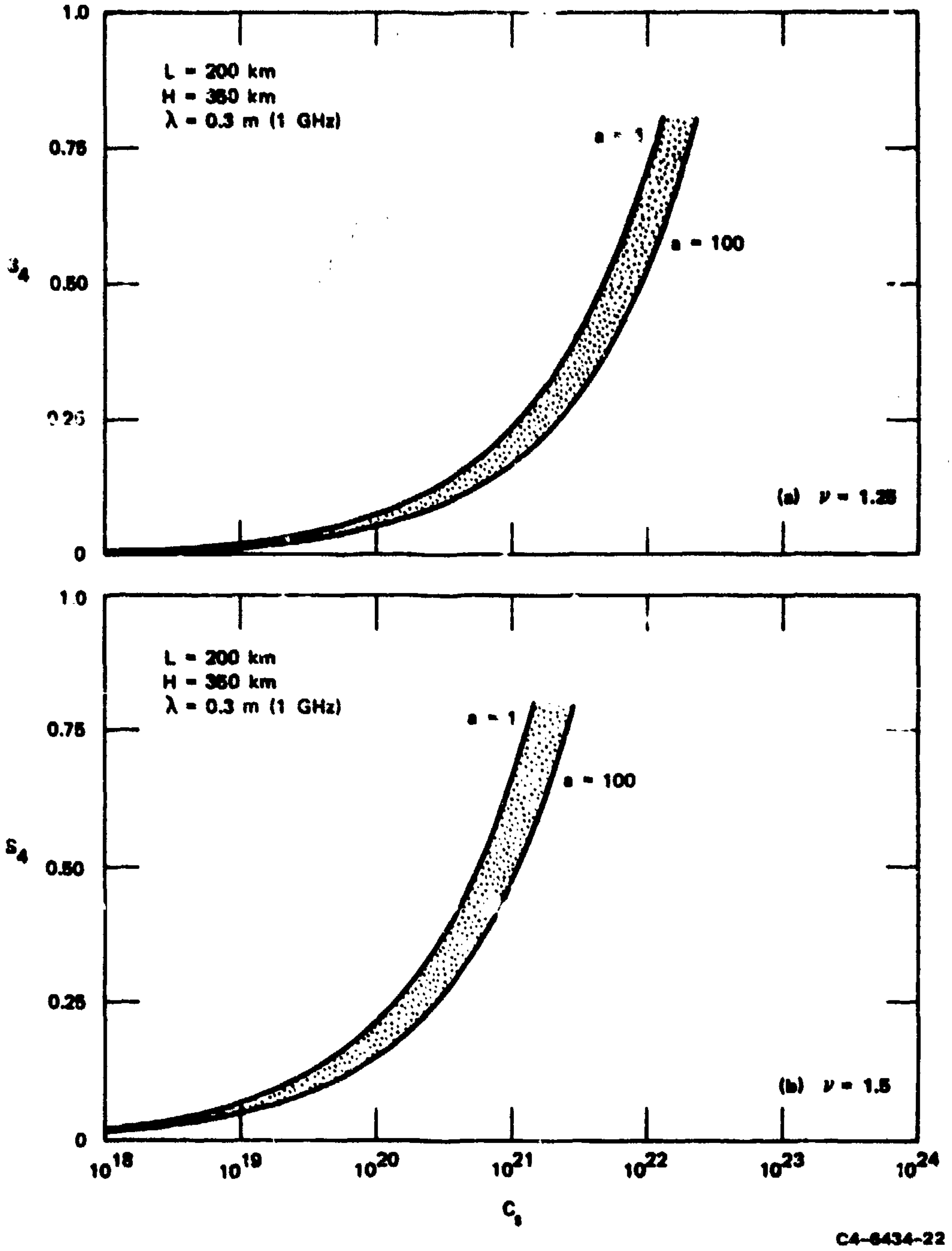

FIGURE 22 CALCULATED GIGAHERTZ SCINTILLATION FOR IDEALIZED EQUATORIAL GEOMETRY

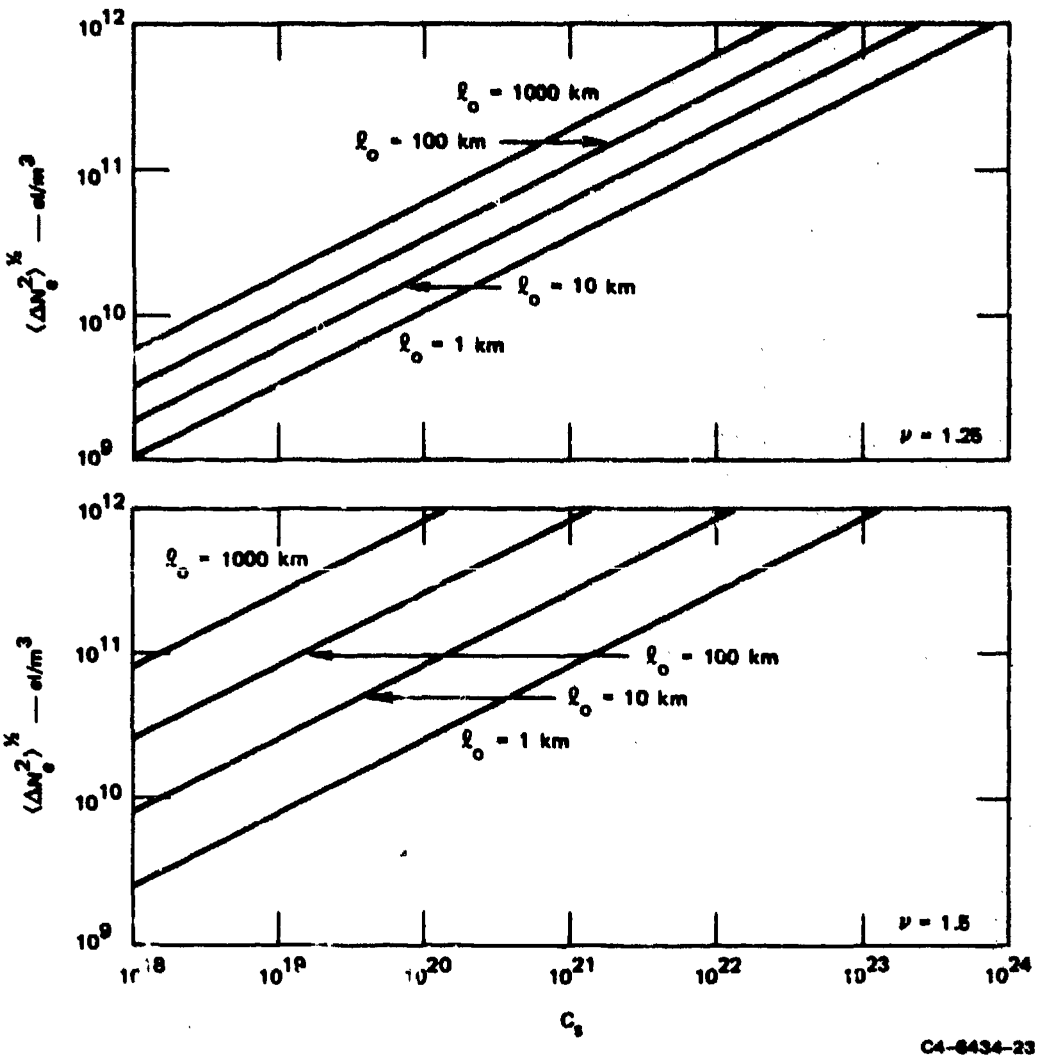

FIGURE 23 RMS ELECTRON DENSITY VARIATION vs STRENGTH OF TURBULENCE FOR DIFFERENT DATA INTERVALS

of less than 10^{12} el/m^3 over 1 to 1000 km data intervals. Significantly smaller values result if the irregularities are extended over a larger region. Thus, we find no inconsistency between our scintillation observations and reported in-situ measurements.

REFERENCES

Basu, S., S. Basu, and B. K. Kahn, "Model of Equatorial Scintillations from In-Situ Measurements," Radio Sci., Vol. 11, No. 10, p. 821 (1976).

Booker, H. G., J. A. Ratcliffe, and D. H. Shinn, "Diffraction from an Irregular Screen with Applications to Ionospheric Problems," Phil. Trans. Roy. Soc., A., Vol. 242, p. 579 (1950).

Bramley, E. N., "The Diffraction of Waves by an Irregular Refracting Medium," Proc. Roy. Soc., A., Vol. 225, p. 515 (1954).

Bramley, E. N., "The Accuracy of Computing Ionospheric Radio-Wave Scintillation by the Thin-Phase-Screen Approximation," J. Atmos. Terr. Phys., Vol. 39, p. 367 (1977).

Briggs, B. H. and I. A. Parkin, "On the Variation of Radio Star and Satellite Scintillations with Zenith Angle," J. Atmos. Terr. Phys., Vol. 25, No. 6, p. 339 (1963).

Buckley, R., "Diffraction by a Random Phase-Changing Screen: A Numerical Experiment," J. Atmos. Terr. Phys., Vol. 37, p. 1431 (1975).

Costa, E. and M. C. Kelley, "Calculations of Equatorial Scintillations at VHF and Gigahertz Frequencies Based on a New Model of the Disturbed Equatorial Ionosphere," Geophys. Res. Lett., Vol. 3, No. 11, p. 677 (1976).

Crane, R., "Spectra of Ionospheric Scintillation," J. Geophys. Res., Vol. 81, p. 2041 (1976).

Crane, R., "Ionospheric Scintillation," Proc. IEEE, Vol. 65, No. 2, p. 180 (1977).

Cronyn, W. M., "The Analysis of Radio Scattering and Space Probe Observations of Small-Scale Structure in the Interplanetary Medium," Astrophys. J., Vol. 161, p. 755 (1970).

Davies, K., R. B. Fritz, R. N. Grubb, and J. E. Jones, "Some Early Results from the ATS-6 Radio Beacon Experiment," Radio Sci., Vol. 10, p. 785 (1975).

Fremouw, E. J., R. L. Leadabrand, R. C. Livingston, M. D. Cousins, C. L. Rino, B. C. Fair, and R. A. Long, "Early Results from the DNA Wideband Satellite Experiment--Complex-Signal Scintillation," Radio Sci., Vol. 13, No. 1, p. 167 (1978).

Gradshteyn, I. S. and I. M. Ryzhik, *Table of Integrals Series and Products* (Academic Press Inc., 111 Fifth Avenue, New York, N.Y., 1965).

Gochelashvili, K. and V. Shishov, "Laser Beam Scintillation Beyond a Turbulent Layer," *Opt. Acta*, Vol. 18, p. 313 (1971).

Leitinger, R., G. Schmidt, and A. Tauriainen, "An Evaluation Method Combining the Differential Doppler Measurements from Two Stations that Enables the Calculation of the Electron Content of the Ionosphere," *J. Geophys. Res.*, Vol. 41, p. 201 (1975).

Livingston, R. C., "Comparative Equatorial Scintillation Morphology--American and Pacific Sectors," Technical Report 3, Contract DNA001-77-C-0220, SRI Project 6434, SRI International, Menlo Park, CA (in preparation, 1978).

Ratcliffe, J. A., "Some Aspects of Diffraction Theory and Their Application to the Ionosphere," *Phys. Soc. Prog. Phys.*, Vol. 19, p. 188 (1956).

Rino, C. L. and E. J. Fremouw, "The Angle Dependence of Singly Scattered Wavefields," *J. Atmos. Terr. Phys.*, Vol. 39, p. 859 (1977).

Rino, C. L. and R. C. Livingston, "A Spaced Receiver Data Analysis Technique for Simultaneously Estimating Anisotropy and Pattern Drifts in Radio Wave Transmission Experiments," Technical Report 4, Contract DNA001-77-C-0220, SRI Project 6434, SRI International, Menlo Park, CA (in preparation, 1978).

Rufenach, C. L., "Ionospheric Scintillation by a R[illegible]om Phase Screen: Spectral Approach," *Radio Sci.*, Vol. 10, p. 1[illegible] (1975).

Rumsey, V. H., "Scintillations Due to a Concentrated Layer with a Power-Law Turbulence Spectrum," *Radio Sci.*, Vol. 10, p. 107 (1975).

Salpeter, E. E., "Interplanetary Scintillations.I--Theory," *Astrophys. J.*, Vol. 147, p. 433 (1967).

Singleton, D. G., "The Dependence of High-Latitude Ionospheric Scintillations on Zenith Angle and Azimuth," *J. Atmos. Terr. Phys.*, Vol. 35, p. 2253 (1973).

Taylor, L. E., "Scintillation of Randomized Electromagnetic Fields," *J. Math. Phys.*, Vol. 13, p. 590 (1972).

Wernik, A. W., "Extinction Effects in the Single Scattering Scintillation Theory," *Publs. Inst. Geoph. Pol. Ac. Sci.*, Vol. E-1, No. 100, p. 43 (1976).

Yeh, K. C. and C. H. Liu, "Diagnosis of the Turbulent State of Ionospheric Plasma by Propagation Methods," *Radio Sci.*, Vol. 12, No. 6, p. 1031 (1977).

Appendix

NOISE CORRECTIONS FOR MEASURED S_4 SCINTILLATION INDEX VALUES

If we apply the conventional model of a singal plus independent additive white Gaussian noise, it is easily shown that the measured scintillation index $\hat{S}_4$ has the form

$$\hat{S}_4 = (S_4^2 + 2SNR^{-1} + SNR^{-2})^{1/2} / (1 + SNR^{-1}) \tag{A-1}$$

where SNR denotes the power signal-to-noise ratio. It is interesting to note that if $S_4 = 1$, then $\hat{S}_4 = 1$ irrespective of SNR.

In general, however, the noise contribution causes $\hat{S}_4$ to be larger than S_4. In Figure A-1 we have plotted the measured scintillation index against S_4 for different SNRs. It can be seen that when $S_4 \leq 0.1$ with SNRs less than 30 dB, a noise correction must be applied. For the Wideband satellite data, the SNR is typically better than 30 dB.

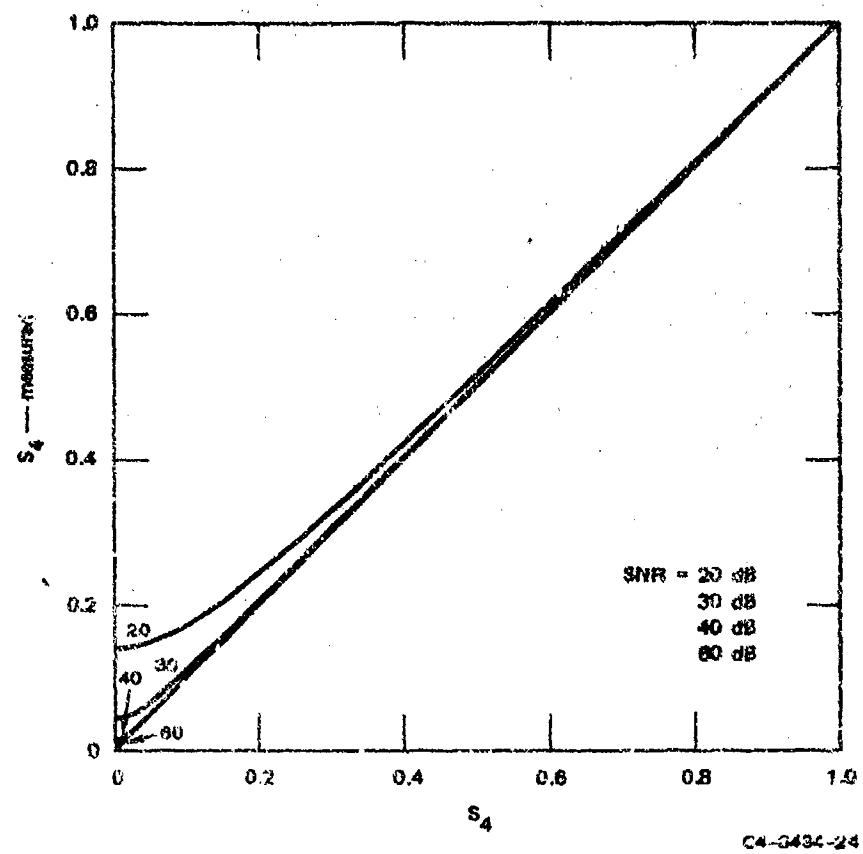

FIGURE A-1 NOISE CONTRIBUTION TO S_4

DISTRIBUTION LIST

DEPARTMENT OF DEFENSE

Assistant Secretary of Defense
Comm, Cmd, Cont. & Intell.
ATTN: J. Babcock
ATTN: M. Epstein

Assistant to the Secretary of Defense
Atomic Energy
ATTN: Executive Assistant

Command & Control Technical Center
ATTN: C-650, W. Heidig
ATTN: C-650, G. Jones
ATTN: C-312, R. Mason

Defense Advanced Rsch. Proj. Agency
ATTN: NMRO
ATTN: STO

Defense Communication Engineer Center
ATTN: Code R410, J. McLean
ATTN: R720, J. Worthington

Defense Communications Agency
ATTN: Code 103, M. Raffensperger
ATTN: Code 480
ATTN: Code 810, R. Rostron
ATTN: Code 101B

Defense Documentation Center
Cameron Station
12 cy ATTN: TC

Defense Intelligence Agency
ATTN: DT-1B
ATTN: DB-4C, E. O'Farrell
ATTN: DIAAP, A. Wise
ATTN: DT-5
ATTN: DB-1SZ, R. [illegible]
ATTN: HQ-TR, J. [illegible]
ATTN: DC-7D, W. [illegible]

Defense Nuclear Agency
ATTN: STVL
ATTN: DDST
3 cy ATTN: RAAE
4 cy ATTN: TITL

Field Command
Defense Nuclear Agency
ATTN: FCPR

Interservice Nuclear Weapons School
ATTN: Document Control

Joint Chiefs of Staff
ATTN: J-3, WWMCCS, Evaluation Office

Joint Strat. Tgt. Planning Staff
ATTN: JPST, G. Goetz
ATTN: JLTW-2

Under Secretary of Def. for Rsch. & Engrg.
ATTN: Strategic & Space Systems (OS)

DEPARTMENT OF DEFENSE (Continued)

Livermore Division, Field Command, DNA
Lawrence Livermore Laboratory
ATTN: FCPRL

National Security Agency
ATTN: F. Leonard
ATTN: W14, P. Clark
ATTN: W32, O. Bartlett
ATTN: R52, J. Skillman
ATTN: R5

DEPARTMENT OF THE ARMY

Atmospheric Sciences Laboratory
U.S. Army Research & Development Command
ATTN: DELAS-EO, F. Niles

Chief C-E Services Division
ATTN: C-E Services Division

ERADCOM Technical Support Activity
ATTN: J. Quigley
ATTN: DRSEL-PL-ENV, H. Bomke

Harry Diamond Laboratories
ATTN: DELHD-NP, C. Moazed
ATTN: DELHD-TI, M. Weiner
ATTN: DELHD-NP, F. Wimenitz
ATTN: DELHD-RB, R. Williams

U.S. Army Ballistic Research Labs.
ATTN: Tech. Lib., E. Baicy

U.S. Army Comm-Elec. Engrg. Instal. Agency
ATTN: CCC-EMEO, W. Nair
ATTN: EED-PED, G. Lane

U.S. Army Foreign Science & Tech. Ctr.
ATTN: DRXST-SD
ATTN: R. Jones

U.S. Army Materiel Dev. & Readiness Cmd.
ATTN: DRCLDC, J. Bender

U.S. Army Nuclear & Chemical Agency
ATTN: Library

U.S. Army Satcom Agency
ATTN: Document Control

U.S. Army TRADOC Systems Analysis Activity
ATTN: ATAA-TAC, J. Hesse
ATTN: ATAA-SA
ATTN: TCC, F. Payan, Jr.

DEPARTMENT OF THE NAVY

Naval Electronic Systems Command
ATTN: PME 117-T
ATTN: NAVALEX 034, T. Hughes
ATTN: Code 5011
ATTN: PME 117

DEPARTMENT OF THE NAVY (Continued)

Naval Intelligence Support Ctr.
ATTN: Code 5404, J. Galet
ATTN: STIC 12, Mr. Dubbin

Naval Ocean Systems Center
ATTN: Code 0230, C. Baggett
ATTN: Code 81, R. Eastman
3 cy ATTN: Code 532, W. Moler

Naval Research Laboratory
ATTN: Code 5400, Hq. Comm. Dir., B. Wald
ATTN: Code 7701, J. Brown
ATTN: Code 5465
ATTN: Code 5410, J. Davis
ATTN: Code 5460
ATTN: Code 5430
ATTN: Code 7700, T. Coffey

Naval Space Surveillance System
ATTN: J. Burton

Naval Space System Activity
ATTN: A. Hazzard

Naval Surface Weapons Center
ATTN: Code F31

Naval Surface Weapons Center
Dahlgren Laboratory
ATTN: Code DF-14, R. Butler

Navy Space Systems Activity
ATTN: Code 52

Office of Naval Research
ATTN: Code 461
ATTN: Code 402
ATTN: Code 420
ATTN: Code 421

Strategic Systems Project Office
ATTN: NSP-2141
ATTN: NSSP-2722, F. Wimberly

DEPARTMENT OF THE AIR FORCE

Aerospace Defense Command/DC
ATTN: DC, Mr. Long

Aerospace Defense Command/XPD
ATTN: XPDQQ
ATTN: XP

Air Force Avionics Laboratory
ATTN: AAD, W. Hunt
ATTN: AAB, H. Hartman
ATTN: AAD, A. Johnson

Air Force Geophysics Laboratory
ATTN: OPR, A. Stair
ATTN: OPR-1, J. Ulwick
ATTN: LKB, K. Champion
ATTN: PHP, J. Aarons
ATTN: PHD, J. Buchau
ATTN: PHD, J. Mullen

Air Force Technical Applications Center
ATTN: TF, Maj Wiley

DEPARTMENT OF THE AIR FORCE (Continued)

Air Force Weapons Laboratory
ATTN: SUL
ATTN: DYC, J. Kamm
ATTN: DYC, J. Barry

Deputy Chief of Staff
Research, Development, & Acq.
ATTN: AFRDQ

Headquarters
Electronic Systems Division/XR
ATTN: XR, J. Deas

Headquarters
Electronic Systems Division/YSEA
ATTN: YSEA

Headquarters
Electronic Systems Division, AFSC
ATTN: J. Whelan
ATTN: XRW

Foreign Technology Division, AFSC
ATTN: NICD, Library
ATTN: ETDP, B. Ballard

Rome Air Development Center, AFSC
ATTN: TSLD, Documents Library
ATTN: OCSE, V. Coyne

Rome Air Development Center, AFSC
ATTN: EEP, A. Lorentzen

Space & Missile Systems Organization/MN
ATTN: MNNL, Lt Col Kennedy

Space & Missile Systems Organization/SK
ATTN: SKA, M. Clavin

Space & Missile Systems Organization/SZ
ATTN: SZJ

Space & Missile Systems Organization/YA
ATTN: YAT, L. Blackwelder

Strategic Air Command/XPFS
ATTN: NRT
ATTN: B. Bauer
ATTN: XPFS, B. Stephan
ATTN: DOK, Chief Scientist

DEPARTMENT OF ENERGY

Department of Energy
Albuquerque Operations Office
ATTN: Doc. Con. for D. Sherwood

Department of Energy
ATTN: Doc. Con. for A. Labowitz

Lawrence Livermore Laboratory
ATTN: Doc. Con. for Technical Information Department Library
ATTN: Doc. Con. for L-46, F. Seward

Los Alamos Scientific Laboratory
ATTN: Doc. Con. for D. Westervelt
ATTN: Doc. Con. for P. Keaton
ATTN: Doc. Con. for R. Taschek

DEPARTMENT OF ENERGY

Office of Military Application
ATTN: Doc. Con. for D. Gale

Sandia Laboratories
Livermore Laboratory
ATTN: Doc. Con. for T. Cook
ATTN: Doc. Con. for B. Murphey

Sandia Laboratories
ATTN: Doc. Con. for Space Project Div.
ATTN: Doc. Con. for D. Dahlgren
ATTN: Doc. Con. for J. Marcin
ATTN: Doc. Con. for A. Thornbrough
ATTN: Doc. Con. for W. Brown
ATTN: Doc. Con. for 3141

OTHER GOVERNMENT AGENCIES

Central Intelligence Agency
ATTN: RD/SI, Rm. 5G48, Hq. Bldg. for OSI/PSTD, Rm. 5, F 19

Department of Commerce
National Bureau of Standards
ATTN: R. Moore

Department of Transportation
Office of the Secretary
ATTN: R. Lewis
ATTN: R. Doherty

Institute for Telecommunications Sciences
National Telecommunications & Info. Admin.
ATTN: D. Crombie
ATTN: A. Jean
ATTN: L. Berry
ATTN: W. Utlaut

NASA
Goddard Space Flight Center
ATTN: P. Corrigan

National Oceanic & Atmospheric Admin.
Environmental Research Laboratories
ATTN: Aeronomy Lab., G. Reid
ATTN: R. Grubb

DEPARTMENT OF DEFENSE CONTRACTORS

Aerospace Corporation
ATTN: F. Morse
ATTN: S. Bower
ATTN: N. Stockwell
ATTN: J. Carter
ATTN: SMFA for PWW
ATTN: I. Garfunkel
ATTN: V. Josephson
ATTN: T. Salmi
ATTN: D. Olsen

Analytical Systems Engineering Corporation
ATTN: Radio Sciences

Berkeley Research Associates, Inc.
ATTN: J. Workman

Brown Engineering Company, Inc.
ATTN: N. Deliberis

DEPARTMENT OF DEFENSE CONTRACTORS (Continued)

Boeing Company
ATTN: G. Keister
ATTN: D. Murray
ATTN: G. Hall
ATTN: J. Kenney

University of California at San Diego
ATTN: H. Booker

Charles Stark Draper Laboratory, Inc.
ATTN: D. Cox
ATTN: J. Gilmore

Computer Sciences Corporation
ATTN: H. Blank

Comsat Labs.
ATTN: G. Hyde

Cornell University
ATTN: D. Farley, Jr.

Electrospace Systems, Inc.
ATTN: H. Logston

ESL, Inc.
ATTN: C. Prettie
ATTN: J. Roberts
ATTN: J. Marshall

Ford Aerospace & Communications Corp.
ATTN: J. Mattingley

General Electric Company
Space Division
ATTN: M. Bortner, Space Sci. Lab.

General Electric Company
ATTN: F. Reibert

General Electric Co.-TEMPO
Center for Advanced Studies
ATTN: M. Stanton
ATTN: W. Knapp
ATTN: T. Stephans
ATTN: D. Chandler
ATTN: B. Gambill
ATTN: DASIAC

General Electric Tech. Services Co., Inc.
ATTN: G. Millman

General Research Corporation
Santa Barbara Division
ATTN: J. Ise, Jr.
ATTN: J. Garbarino

Geophysical Institute
University of Alaska
ATTN: T. Davis
ATTN: Technical Library
ATTN: N. Brown

GTE Sylvania, Inc.
Electronics Systems Grp-Eastern Div.
ATTN: M. Cross

HSS, Inc.
ATTN: D. Hansen

DEPARTMENT OF DEFENSE CONTRACTORS (Continued)

University of Illinois
Department of Electrical Engineering
ATTN: K. Yeh

Institute for Defense Analyses
ATTN: J. Aein
ATTN: E. Bauer
ATTN: H. Wolfhard
ATTN: J. Bengston

International Tel. & Telegraph Corp.
ATTN: Technical Library

JAYCOR
ATTN: S. Goldman

Johns Hopkins University
Applied Physics Lab.
ATTN: T. Potemra
ATTN: Document Librarian
ATTN: J. Dassoulas

Kaman Sciences Corporation
ATTN: T. Meagher

Linkabit Corporation
ATTN: I. Jacobs

Lockheed Missiles & Space Co., Inc.
ATTN: D. Churchill
ATTN: Dept. 60-12

Lockheed Missiles & Space Co., Inc.
ATTN: D/52-12, W. Imhof
ATTN: D/52-12, R. Johnson
ATTN: D/52-10, M. Walt

MIT Lincoln Lab.
ATTN: P. Waldron
ATTN: L. Loughlin
ATTN: D. Towle
ATTN: D. Clark

McDonnell Douglas Corp.
ATTN: G. Mroz
ATTN: W. Olson
ATTN: J. Moule
ATTN: N. Harris

Mission Research Corp.
ATTN: S. Gutsche
ATTN: D. Sowle
ATTN: F. Fajen
ATTN: R. Hendrick
ATTN: M. Scheibe
ATTN: R. Bogusch
ATTN: P. Fischer

Mitre Corp.
ATTN: J. Morganstern
ATTN: G. Harding
ATTN: C. Callahan

Mitre Corp.
ATTN: W. Hall
ATTN: W. Foster

Pacific-Sierra Research Corp.
ATTN: E. Field, Jr.

Pennsylvania State University
Ionosphere Research Lab.
ATTN: Ionospheric Research Lab.

Photometrics, Inc.
ATTN: I. Kofsky

Physical Dynamics, Inc.
ATTN: A. Thompson

Physical Dynamics, Inc.
ATTN: E. Fremouw

R&D Associates
ATTN: C. MacDonald
ATTN: W. Karzas
ATTN: W. Wright, Jr.
ATTN: R. Lelevier
ATTN: H. Ory
ATTN: F. Gilmore
ATTN: B. Gabbard
ATTN: R. Turco

Rand Corporation
ATTN: E. Bedrozian
ATTN: C. Crain

Raytheon Company
ATTN: B. Adams

Riverside Research Institute
ATTN: V. Trapani

Science Applications, Inc.
ATTN: C. Smith
ATTN: L. Linson
ATTN: D. Sachs
ATTN: D. Hamlin
ATTN: E. Straker
ATTN: J. McDougall

Science Applications, Inc.
Huntsville Division
ATTN: D. Divis

Science Applications, Inc.
ATTN: SZ

SRI International
2 cy ATTN: W. Jaye//L. Cobb
2 cy ATTN: D. Johnson//D. Neilson
3 cy ATTN: J. Peterson//G. Price//A. Burns
ATTN: C. Rino
ATTN: S. Matthews
ATTN: W. Chesnut
ATTN: G. Smith
ATTN: R. Leadabrand
ATTN: M. Baron
ATTN: G. Carpenter

Tri-Com., Inc.
ATTN: D. Murray

TRW Defense & Space Sys. Group
ATTN: D. Dee
ATTN: R. Plebuch
ATTN: S. Altschuler

VisiDyne, Inc.
ATTN: C. Humphrey
ATTN: J. Carpenter